ORIGINAL ARTICLE

Journal Section

Revisiting the Relation Between Momentum and Scalar Roughness Lengths of Urban Surfaces

Qi Li[1*2] | **Elie Bou-Zeid**[2] | **Sue Grimmond**[3] | **Sergej Zilitinkevich**[4] | **Gabriel Katul**[5,6,2]

[1]School of Civil and Environmental Engineering, Ithaca, NY, USA

[2]Department of Civil and Environmental Engineering, Princeton, NJ, USA

[3]Department of Meteorology, University of Reading, Reading, UK

[4]Finnish Meteorological Institute, P.O. Box 503, 00101 Helsinki, Finland

[5]Nicholas School of the Environment, Duke University, Durham, NC, USA

[6]Department of Civil and Environmental Engineering, Duke University, Durham, NC, USA

Correspondence
Email: ql56@cornell.edu

Funding information
Support was provided by start-up funds from Cornell University; the small allocation grant for new faculty by the National Center for Atmospheric Research (NCAR), NOAA-Princeton Cooperative Institute for Climate Science (CU00029), Princeton's Andlinger Center for Energy and the Environment, and the U.S. National Science Foundation (NSF) Sustainability Research Network (Cooperative Agreement 1444758 and grant 1664091). High-performance computing support from Cheyenne (doi:10.5065/D6RX99HX) provided by NCAR's Computational and Information Systems Laboratory (NSF projects P36861020 and UPRI0007) is acknowledged. SZ acknowledges support from the Academy of Finland (grant 314 798/799), and GK acknowledges partial support from NSF-AGS-1644382 and NSF-IOS-1754893. The Metropolis Project is acknowledged for supporting the collaborative visit of GK to Princeton University.

Large Eddy Simulations (LES) of neutral flow over regular

arrays of cuboids are conducted to explore connections between momentum (z_{0m}) and scalar (z_{0s}) roughness lengths in urban environments, and how they are influenced by surface geometry. As LES resolves the obstacles but not the micro-scale boundary layers attached to them, the aforementioned roughness lengths are analyzed at two distinct spatial scales. At the micro-scale (roughness of individual facets, e.g. roofs), it is assumed that both momentum and scalar transfer are governed by accepted arguments for smooth walls that form the basis for the LES wall model. At the macro-scale, the roughness lengths are representative of the aggregate effects of momentum and scalar transfer over the resolved roughness elements of the whole surface, and hence they are directly computed from the LES. The results indicate that morphologically-based parameterizations for macro-scale z_{0m} are adequate overall. The relation between the momentum and scalar macro-roughness values, as conventionally represented by $\log(z_{0m}/z_{0s})$ and assumed to scale with Re_*^n (where Re_* is a roughness Reynolds number), is then interpreted using surface renewal theory (SRT). SRT predicts $n = 1/4$ when only Kolmogorov-scale eddies dominate the scalar exchange, whereas $n = 1/2$ is predicted when large eddies limit the renewal dynamics. The latter is found to better capture the LES results. However, both scaling relations indicate that z_{0s} decreases when z_{0m} increases for typical urban geometries and scales. This is opposite to how their relation is usually modeled for urban canopies (i.e. z_{0s}/z_{0m} is a fixed value smaller than unity).

KEYWORDS
large-eddy simulation, scalar roughness length, surface renewal theory, urban canopy

1 | INTRODUCTION

1.1 | Overview of roughness lengths

Quantification of momentum, heat, water vapor and other trace gas fluxes over built surfaces remains a first-order challenge in modeling and observation of urban climates and meteorology (Masson, 2000; Grimmond and Oke, 2002;

Bou-Zeid et al., 2009; Llaguno-Munitxa and Bou-Zeid, 2018). Monin-Obukhov similarity theory (MOST) (Monin and Obukhov, 1954) remains the cornerstone for representing these turbulent exchanges between the earth surface and the lower atmosphere although possible refinements accounting for deviations from MOST in the roughness sublayer have been proposed for urban (Theeuwes et al., 2019) and vegetated canopies (Garratt, 1980; Harman and Finnigan, 2007, 2008). The roughness lengths used in MOST are of significance in coupled urban-atmospheric models: they encapsulate how turbulent exchanges depend on the characteristics of the underlying surface such as geometric or thermal properties, and on the spatial distributions of scalar sources/sinks at the surface (Garratt, 1992). In MOST, the momentum and scalar roughness lengths (z_{0m} and z_{0s}) for neutral atmospheric flows are used to determine the surface drag (represented by the friction velocity u_*) and scalar fluxes (represented by the scalar, here temperature, scale θ_*) based on the mean profiles of streamwise velocity $\bar{u}$ and temperature $\bar{\theta}$ via

$$u_* = \bar{u}\left[\frac{1}{\kappa}\log\left(\frac{z-d}{z_{0m}}\right)\right]^{-1} \tag{1}$$

and

$$\theta_* = (\bar{\theta}_s - \bar{\theta})\left[\frac{1}{\kappa}\log\left(\frac{z-d_s}{z_{0s}}\right)\right]^{-1}, \tag{2}$$

where κ is the von Kármán constant (κ is assumed to be 0.4); d and d_s are the displacement heights of momentum and scalars, respectively; $\bar{\theta}_s$ is the 'aerodynamic' mean surface temperature, which is obtained by extending the scalar logarithmic profile to $z = z_{0s} + d_s$; u_* is the friction velocity; and $\theta_* = F_c/u_*$ where F_c is the kinematic surface scalar flux (here sensible heat flux).

Roughness lengths and corollary concepts such as friction factor have been extensively studied in both the engineering and the atmospheric sciences communities since the early 20th century. Rough-wall turbulent boundary layers were examined in the classic experiments by Nikuradse (1933) for turbulent flows over sand roughness covering the walls of a pipe in the absence of buoyancy forces. Since then, the concept of 'roughness function' has been an active area of research in the engineering community (Perry et al., 1969; Flack and Schultz, 2014). In hydrology, the distinction between z_{0m} and z_{0s} over a variety of natural surfaces gained significant research attention with the proliferation of remote-sensing platforms that now will skin temperature at high spatial and temporal resolution (Schmugge et al., 2002; Morrison et al., 2020). Early analysis by Brutsaert (1975b) showed that scalar transfer differs for smooth and rough natural surfaces despite the fact that both are driven by molecular exchange. For a rough surface, it is now well established that z_{0m} and z_{0s} are not equal (Garratt, 1992, Chap.4). Similarity between turbulent transport of momentum and scalars (i.e. the Reynolds analogy) is generally valid for high Reynolds number (Re) flows (Yang and Abkar, 2018), thus justifying the existence of a logarithmic layer for a passive scalar in Eq. 2. However, inequality between z_{0m} and z_{0s} still arises because in the 'immediate vicinity' of the wall (Brutsaert, 1975a), (i.e. the interfacial sublayer between the fluid and surface of the roughness elements), the mechanisms of scalar and momentum transfer differ. While scalar transfer relies on molecular diffusion, momentum transfer is dominated at high Re by pressure (or form) drag in addition to the viscous drag (Brutsaert, 1975a,b).

Conventionally, z_{0s} is related to z_{0m} using the quantity $\kappa B^{-1} = \log(z_{0m}/z_{0s})$ (Owen and Thomson, 1963; Garratt, 1992) because of the large variations expected in z_{0m}/z_{0s}. Although it is less discussed in the literature, d and d_s may also be unequal if momentum sinks and scalar sources/sinks drastically differ when eddy penetration into roughness elements is incomplete (Siqueira and Katul, 2010). Finally, roughness length concepts extend beyond the framework of MOST. Roughness lengths are indispensable model parameters when using the aerodynamic resistance approach

(ARM), which is ubiquitously applied in various subfields of meteorology (Lhomme, 1991) and in common schemes to compute surface fluxes in mesoscale numerical weather models (Chen et al., 2010; Chen and Zhang, 2009).

1.2 | Roughness lengths for urban rough surfaces

For context, previous work linking z_{0m} and z_{0s} to geometric features of urban rough surfaces is briefly reviewed. Emphasis is placed on z_{0s} because fewer studies on scalar roughness lengths over urban surfaces have been presented compared to momentum, despite their significance for turbulent fluxes in urban land-atmosphere models (Demuzere et al., 2008; Ryu et al., 2011; Wang et al., 2013; Li and Bou-Zeid, 2014). It is to be noted that roughness length models derived for vegetated canopies may not be directly extrapolated to urban surfaces. Buildings are bluff roughness elements that distinctly impact the flow when compared to permeable plants. Furthermore, the spatially heterogeneous surface temperatures and distributions of scalar sources/sinks within urban rough surfaces makes the problem of scalar roughness length determination a formidable challenge (Voogt and Grimmond, 2000; Kanda et al., 2007; Crawford et al., 2018). Nevertheless, this is a challenge that cannot be overlooked. It is of practical interest to determine z_{0m}, z_{0s}, and the corresponding bulk transfer coefficients over bluff-rough surfaces by relating them to directly-measurable surface geometrical properties (Kastner-Klein and Rotach, 2004; De Ridder, 2006; Kanda et al., 2007; Demuzere et al., 2008; Kanda et al., 2013; Zhu and Anderson, 2018). For z_{0m}, significant progress has been achieved on this front (Macdonald et al., 1998; Grimmond and Oke, 1999; Barlow and Coceal, 2009; Kanda et al., 2013; Yang et al., 2016; Kent et al., 2017; Yang et al., 2019; Zhu and Anderson, 2018) and reviewing all this literature is beyond the scope of the work here. For z_{0s}, the common approach is to relate it to z_{0m} using the quantity κB^{-1} that is assumed to vary only with the roughness Reynolds number, $Re^* = u_* z_{0m}/\nu$, where ν is the kinematic viscosity and u_* is an effective friction velocity for the urban boundary layer. However, determining this relation $\kappa B^{-1} = f(Re^*)$ so as to obtain z_{0s} remains difficult.

Semi-idealized field experiments using an outdoor scale-model have allowed some progress to be made (Kanda et al., 2007). In terms of the geometric effects on scalar transport, it was shown (Kanda et al., 2007) that κB^{-1} follows a universal parameterization based on a model by Brutsaert (1982) even for surfaces of different geometries. One limitation of such semi-idealized experiments is that they cannot capture other known factors that contribute to the variability of κB^{-1} such as inhomogeneous distributions of heat sources and water vapor availability as reported in field experiments at a suburban site in Tokyo, Japan (Moriwaki and Kanda, 2006a). Furthermore, vegetation fraction and anthropogenic heat sources have been shown to impact roughness parameterization (Crawford et al., 2018) but these elements were not represented in scale-model experiments. Field experiments conducted at actual urban sites face daunting challenges as well. It has been demonstrated (Voogt and Grimmond, 2000) that uncertainties related to different methodologies of surface temperature determination influence the calculated value of κB^{-1}. In addition to field experiments, wind-tunnel experiments on bluff-bodies that are heated or coated with a passive scalar have also been used for roughness length studies. For instance, cuboids coated with naphthalene (Barlow et al., 2004) or wetted with water (Ikegaya et al., 2012; Chung et al., 2015) were used to investigate the dependence of scalar transfer coefficients on roughness packing density, height variations, orientations and distributions of scalar sources.

Numerical approaches such as large eddy simulations (LES) are increasingly used to tackle this problems as well. Anderson (2013) simulated flow and scalar transport over different fractal surfaces finding that the usually-assumed constant value for κB^{-1} does not hold over the range of $Re_* = 10{-}300$. This range encompasses aerodynamically rough morphologies often encountered in the atmospheric boundary layer, except for urban morphologies. Uncertainties are invariably associated with using numerical simulations over rough walls. In particular, wall-modeled LES, which is usually applied for simulating flows in the atmospheric boundary layer, does not resolve the viscous sublayer or the

interfacial layer for each facet. Thus, molecular mass and heat diffusion that occurs at the interface between air and the surface of the roughness elements needs to be modeled. Wall-modeled LES is currently viewed as a leading numerical technique that is able to preserve the high Re of the atmosphere. Unlike momentum transfer studies where the flow becomes Reynolds number independent beyond a certain high Re threshold, matching the elevated Re expected in the atmosphere has been shown to be necessary when exploring scalar transfer and its connection to momentum transfer (Li et al., 2016b).

Numerical experiments using LES over surfaces of different geometries are conducted here to address two research objectives: the first is to examine the implications of using wall-modeled LES to infer macro-scale scalar roughness length, and the second is to determine the scaling between κB^{-1} and Re^* and how it might depend on the geometric parameters of the rough surface. To address these two objectives, the problem (Section 2) is investigated by using LES results on roughness lengths for different surface geometries (Section 3). The implications on scalar roughness length parameterization using surface renewal theory (Section 4) are discussed prior to the summary and conclusions being drawn (Section 5).

2 | METHOD

2.1 | LES and roughness lengths

LES is a common technique that is widely used to simulate turbulent flow and transport over urban terrain (Kanda et al., 2004; Bou-Zeid et al., 2009; Giometto et al., 2016). Direct numerical simulations (DNS), while preferred, cannot attain sufficiently high $Re_b = u_* \delta_{bl}/\nu$ values representative of the atmospheric boundary layer (Slotnick et al., 2014; Li et al., 2016b), where δ_{bl} is the boundary layer depth. The LES code employed here solves the equations of conservation of total mass, momentum (excluding the Coriolis force), and scalar mass or thermal energy. Buildings are represented using the immersed-boundary method (Appendix A). The scalar selected here is temperature. While temperature is not a passive scalar *per se* and buoyancy forces could arise, we simply omit the buoyancy force term from the vertical momentum equation to simulate a passive scalar in this study (i.e. the role of buoyancy remains to be explored). A constant temperature (=330K) is applied to all solid surfaces, as an input to a wall-model for LES (see Eq. 4) as the scalar boundary condition. However, real buildings have neither constant temperature nor flux. Use of more realistic boundary conditions (e.g. coupling building energy models and radiative heat exchanges on the exterior surfaces) is left for future study.

Two different representations of roughness lengths must be clarified. As indicated in Fig. 1, within the urban boundary layer (hereafter *macro-scale*) roughness lengths z_{0m}^{mac} and z_{0s}^{mac}, as well as the zero-plane displacements, are manifestations of the aggregate effects of the bluff-rough surfaces on the inertial sublayer aloft, where the logarithmic mean velocity and mean air temperature profiles hold. (e.g. (Kanda et al., 2013; Yang et al., 2016)) macro-scale thermal roughness lengths for flows over steep ocean waves (Sullivan et al., 2017). This needs to be distinguished from each single building facet's (e.g. a roof) boundary-layer (hereafter micro-scale) roughness parameters. The micro-scale roughness is associated with its own local velocity and temperature distribution near the surface, which follow a micro-scale log-law but only in regions where the flow is facet-parallel and in equilibrium with the adjacent surface. These micro-scale roughness and boundary layers in high-Re wall-modeled LES cannot be resolved (Pope, 2000), and require parameterization supplied as a wall model formulation (Li et al., 2016b). Examples of such micro roughness include subgrid-scale wind ripples on resolved waves (Sullivan et al., 2017) and small indentations on the surfaces of built structures (Cai, 2012; Li et al., 2016b), to name a few. To add to the difficulty of the problem, it is well established that the surface heat exchange parameterized using a wall model, and consequently the flow over an urban canopy, are

sensitive to specification of the micro-scale thermal roughness length (Cai, 2012). Therefore, if one aims to determine the macro-scale roughness length, an evaluation of the parameterization of the micro-scale exchanges is required.

To simplify this problem within the confines of LES, the micro-scale roughness elements are assumed to be smaller than the depth of the local viscous sublayer attached to building facets such that the LES work focuses on the macro-scale. This simplification is akin to setting all building facets as smooth walls. For an aerodynamically smooth surface in the absence of buoyancy forces, the wall-models for momentum and scalar to be used in the LES can be expressed as

$$u_*^{wm} = \frac{\kappa u}{\log \frac{z}{z_{0m}^{mic}}}, \tag{3}$$

$$\theta_*^{wm} = \frac{\kappa \Delta\theta}{\log \frac{z}{z_{0s}^{mic}}}, \tag{4}$$

where the superscript wm represents the wall-modeled quantities of surface stress and scalar flux $F_s = u_*^{wm}\theta_*^{wm}$; $\Delta\theta$ is the difference between θ at the surface and at the first grid point away from the wall (where the flow is assumed to be already fully turbulent); and u is the wall-parallel fluid velocity at that same first grid point. The micro-scale roughness lengths z_{0m}^{mic} and z_{0s}^{mic} are set as

$$z_{0m}^{mic} = \frac{1}{9}\frac{\nu}{u_*^{wm}}, \quad z_{0s}^{mic} = \frac{1}{Sc} z_{0m}^{mic}, \tag{5}$$

where the constant 9 is obtained from experiments (Kader and Yaglom, 1972), $Sc = \nu/D_m$ is the molecular Schmidt number set to unity for simplicity here and D_m is the molecular diffusion coefficient for the scalar of interest. Hence, at the micro-scale, the LES assumes $z_{0m}^{mic} = z_{0s}^{mic}$. To be clear, such an LES parameterization does not resolve the viscous sublayer and does not capture the turbulence disequilibrium as the mean flow meanders around the buildings (at the micro-scale), and as such it cannot be an exact model. Log-law wall models are only accurate if the grid point nearest to the facet is within its equilibrium layer; this should hold over most of the facet areas but might be less accurate near transitions and edges. However, previous evaluation of this model for roughness elements with smooth facets indicate that it is adequate for the present purposes (Li et al., 2016b). The aim here is not to refine such wall models in the LES, which continues to be a formidable challenge (Bose and Park, 2018). Rather, the goal is to examine the implications of the aforementioned wall-model on the macro-scale scalar roughness problem with a lens on kB^{-1}.

2.2 | Simulation cases

The details about the LES code are provided in Appendix A and references therein. The grid resolution of the current setup is able to resolve the geometry of the obstacles as for most runs the number of grids resolving one obstacle is greater than six points, as shown to be sufficient with a similar code (Tseng et al., 2006). Sensitivity analysis performed for case VF32 (Li and Bou-Zeid, 2019) found all quantities relevant for computing the scalar and momentum displacement heights and roughness lengths change by less than 6% when the resolution is doubled. Thus, we use the current setup to allow the parameter space to be finely addressed with a reasonable computational cost.

Three categories of urban forms with different plan area density (=λ_p) and frontal area density (=λ_f) are considered.

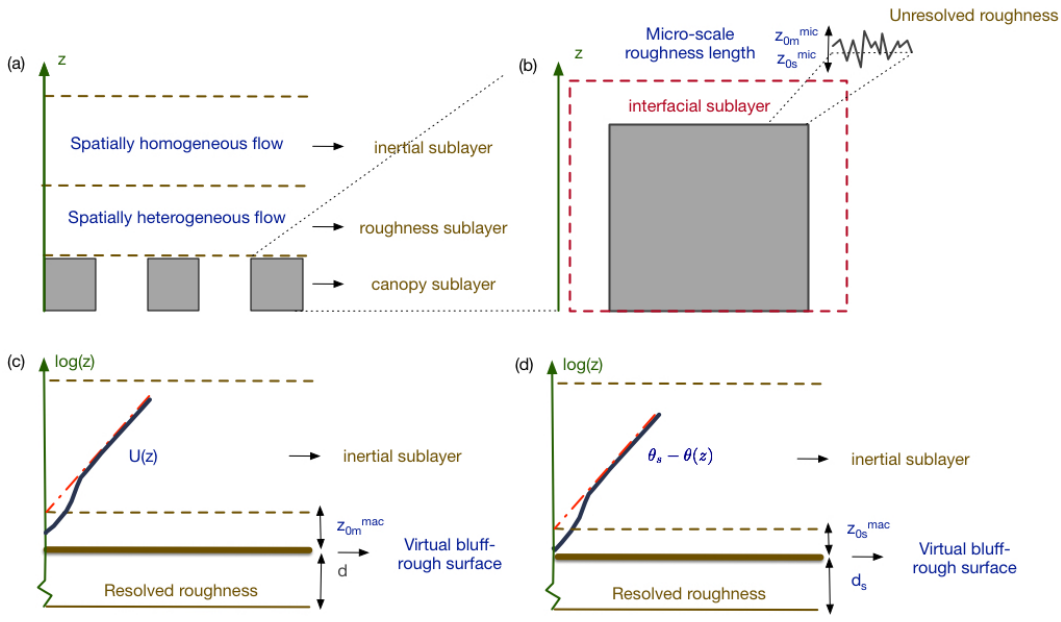

FIGURE 1 Schematic illustration of micro-scale and macro-scale roughness lengths in the LES. The LES resolves the bluff bodies present in the canopy sublayer in (a) but the facet-specific roughness elements shown in (b) are unresolved and must be represented using a wall-model of the interfacial sublayer. The micro-scale roughness lengths are imposed or parameterized in the wall model. The macro-scale roughness lengths for momentum (c) and scalar (d) have virtual origins of the logarithmic profiles of average $\langle u \rangle$ and $\langle \theta_s - \theta \rangle$. The d and d_s define the "virtual bluff-rough" surfaces that represent the aggregate effects of the resolved roughness elements. Notation is defined in the text.

First, (figure 2a), λ_p and λ_f are varied simultaneously but with $\lambda_p = \lambda_f$ hereafter "**V**ariable **P**lan and **F**rontal area density" (VPF). Second (figure 2b), λ_f is maintained constant at 0.25 but λ_p is varied (**V**ariable **P**lan area density, VP). Third (figure 2c), λ_p is kept constant at 0.12 but λ_f is varied (**V**ariable **F**rontal area density, VF). An empirical quadratic relation between λ_f and λ_p derived from Japanese building data (Kanda et al., 2013) found appreciable scatter particularly for non-Japanese cities for fixed λ_p (see their Figure 2). Hence, the category VF explores the effect of such scattered λ_f at a preset fixed λ_p. The simulation parameters for the various cases are summarized in Table 1. The focus is on the parameter space where the two characteristic densities fall between 0.1 and 0.5, reflecting the expected values for many cities and districts (Kanda et al., 2013).

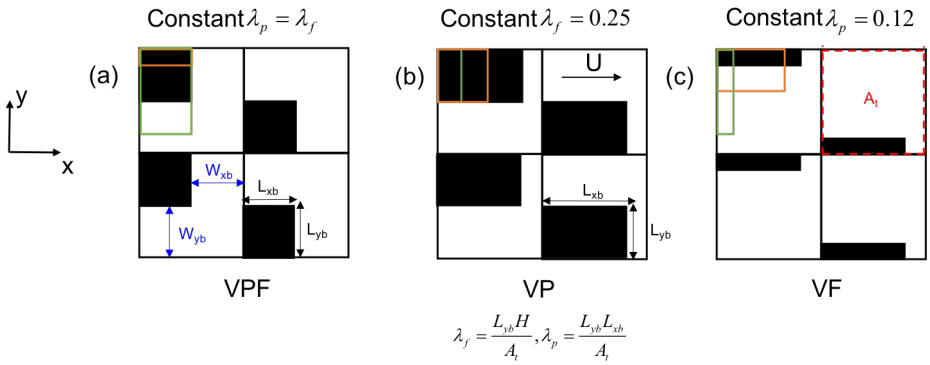

FIGURE 2 Plan area view of one "repeating unit" consisting of four buildings (black) as different geometries with a height (H) of 12.5 m. The black, orange and green lines illustrate three different possible variations of geometry within each category. (a) Variable plan and frontal area **VPF**; (b) Variable plan at a constant frontal area **VP**; (c) Variable frontal area at a constant plan area **VF**. The dimensions of the repeating units, $D_x \times D_y$, are $0.5\delta \times 0.5\delta$, $0.5\delta \times 0.5\delta$ and $0.625\delta \times 0.625\delta$ in VPF, VP and VF, respectively (see Table 1). L_{xb} and L_{yb} are the dimensions of the obstacles in the x and y directions; W_{xb} and W_{yb} are distances between adjacent obstacles in the x and y directions. Notice that for all cases $W_{xb} + L_{xb} = W_{yb} + L_{yb} = D_x = D_y$.

3 | ROUGHNESS LENGTHS DETERMINED FROM LES

Selected examples of the profiles of horizontally-averaged $\langle \bar{u} \rangle / u_*$ and $\langle (\bar{\theta}_s - \bar{\theta}) \rangle / \theta_*$ are illustrated in Fig. 3 for the VPF, VP and VF categories. Although a least-square fitting procedure to the log-law is a common approach to determine roughness lengths and displacement height (Kanda et al., 2004; Bou-Zeid et al., 2009; Kanda et al., 2013; Placidi and Ganapathisubramani, 2015; Yang et al., 2016). we use a 'brute-force' global parameter search in the d/H - z_{0m}/H parameter space. Additionally, $z_{0m}/H < d/H$ can be enforced when searching all parameter combinations. The optimal z_{0m}/H and d/H parameters that best fit the pre-normalized velocity $\langle \bar{u} \rangle / u_*$ (angled brackets indicate spatial averaging) are those that yield a minimum root-mean-squared error (RMSE) over the range $1.25 \leq z/H \leq 2.25$. The results and conclusions are robust to the choice of logarithmic region to perform the fitting procedure. A sensitivity analysis to the fitting range in the log-layer is shown in Appendix C; maximum deviations at the extreme fitting ranges are less than 40% relative to the adopted ranges. For all these calculations, $\kappa = 0.4$. For notational simplicity, superscripts of macro-scale roughness length are omitted. Different procedures can lead to different computed values for d (Leonardi and Castro, 2010) and consequently of z_{0m}. For example, the "drag force moment" approach to calculate

Case	λ_p	λ_f	$\sum_i \lambda_i$	N_x^b, N_y^b, N_z^b	N_x, N_y, N_z	Re_*
VPF12	0.125	0.125	1.75	8, 4, 8	192, 96, 64	21250
VPF18	0.1875	0.1875	1.87	8, 6, 8	192, 96, 64	42930
VPF25	0.25	0.25	2	8, 8, 8	192, 96, 64	49160
VPF31	0.3125	0.3125	2.12	8, 10, 8	192, 96, 64	36290
VPF37	0.3725	0.3725	2.25	8, 12, 8	192, 96, 64	34910
VPF43	0.4375	0.4375	2.375	8, 14, 8	192, 96, 64	14096
VP12	0.125	0.25	1.75	4, 8, 8	192, 96, 64	88750
VP18	0.1875	0.25	1.875	6, 8, 8	192, 96, 64	70860
VP25	0.25	0.25	2	8, 8, 8	192, 96, 64	49160
VP31	0.3125	0.25	2.125	10, 8, 8	192, 96, 64	48220
VP43	0.4375	0.25	2.375	14, 8, 8	192, 96, 64	17850
VF08	0.12	0.08	1.76	12, 4, 8	200, 100, 64	9770
VF12	0.12	0.12	1.64	8, 6, 8	200, 100, 64	35850
VF16	0.12	0.16	1.56	6, 8, 8	200, 100, 64	78740
VF24	0.12	0.24	1.56	4, 12, 8	200, 100, 64	16504
VF32	0.12	0.32	1.64	3, 16, 8	200, 100, 64	16009

TABLE 1 Summary of simulation parameters: N_i^b is the number of nodes resolving one obstacle and N_i is the total number of nodes for the entire domain in the i direction ($i = 1$ is x or longitudinal direction, $i = 2$ is y or lateral direction and $i = 3$ is z or vertical direction). The number of nodes resolving the repeating units of dimensions $D_x \times D_y$ are 32× 32, 32 × 32 and 40 × 40 for VPF, VP and VF, respectively, where V is 'variable', P is 'plan' and F is 'frontal' area; and the last two digits represent the first two decimal values of λ_p or λ_f. $Re_* = u_* z_{0m}/\nu$, where u_* is $\sqrt{-\langle \overline{u'w'} \rangle}$ defined at z/H=1.5 and ν is kinematic viscosity. Dimension of the computational domain normalized by the boundary layer height δ is L_x/δ =3.0,L_y/δ=1.5,L_z/δ=1 in cases VPF and VP; L_x/δ =3.125,L_y/δ=1.5625,L_z/δ=1 in cases VF.

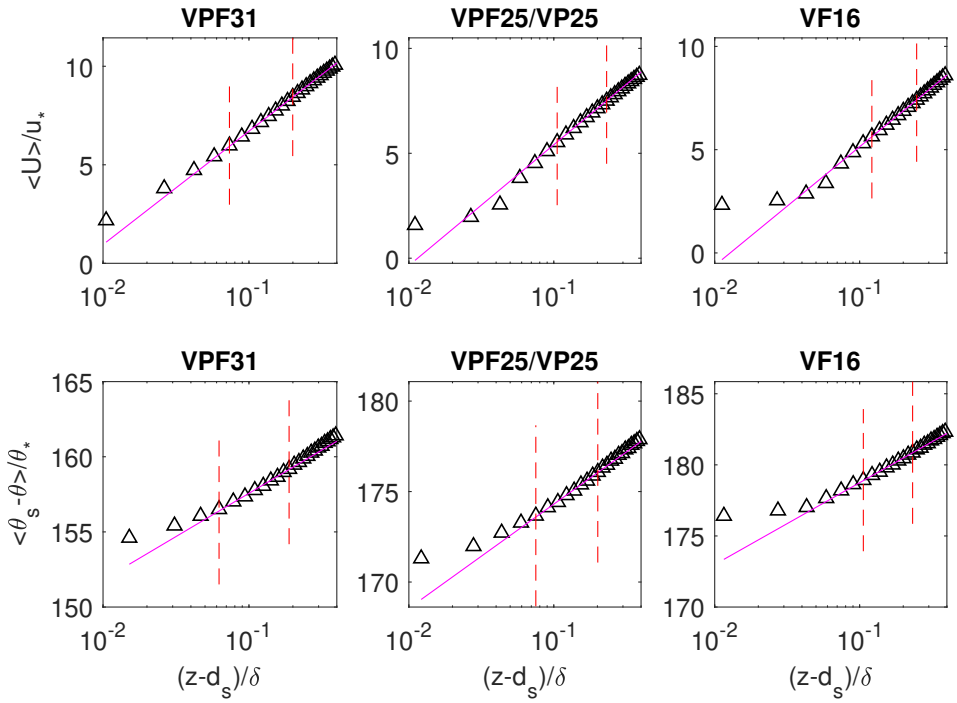

FIGURE 3 $\langle \bar{u} \rangle / u_*$ and $\left\langle (\bar{\theta_s} - \bar{\theta}) \right\rangle / \theta_*$ for three selected cases from the VPF, VP and VF, categories (V variable, P plan and F for frontal area). The log-law region from z/H=1.25 to 2.25 (red dotted vertical lines) indicate the log-lawsobtained from the fitting procedure (magenta solid lines).

d (Jackson, 1981) and other approaches are discussed (Leonardi and Castro, 2010). As the methodology selected only have minor impact on the the momentum and scalar roughness lengths (Appendix C), it is not explored further in this study. Given the minor differences between d and d_s and minor influence on the deduced scalar roughness length, the z_{0s} is determined with $d_s = d$ (reducing the degrees of freedom in roughness length parameterizations). The densest case VP case has a d/H around unity (or slightly larger). This can be attributed to pressure drag effects extending above H, or to uncertainty in the fitting procedure. Using a von Kármán constant (κ) of 0.4, Kanda et al. (2013) found a higher d than adopting a variable κ.

For comparison, two models of d and z_{0m} (Macdonald et al., 1998; Kanda et al., 2013) are featured in Fig. 4. At low λ_f, there are significant differences in predicting d (both models assume d does not vary with λ_f although the LES results suggest it does), particularly for the Macdonald et al. (1998) model (Fig. 4f). The two models predict a decline in z_{0m} with increasing λ_f and decreasing λ_p, consistent with the LES-inferred values. The two-parameter (λ_p and λ_f) Macdonald et al. (1998) model surprisingly captures the responses of z_{0m} to such variable geometries considered in the LES runs (even though it failed to predict d). The surface geometries in our study fall in Mcdonald et al.'s (1998) 'dense regime' (i.e. $\lambda_f > 0.03$) for all cases. The Kanda et al. (2013) model performs better overall when both d and z_{0m} are considered. For realistic highly-heterogeneous urban morphologies, more sophisticated modeling may be required. In such complex canopies, the models might need to explicitly account for the mutual interaction between roughness elements (Yang et al., 2016), or for additional statistical properties of the rough surface such as building height variance or skewness (Kanda et al., 2013; Zhu et al., 2017). Nevertheless, a morphometrically-based model appears viable to estimate z_{0m}.

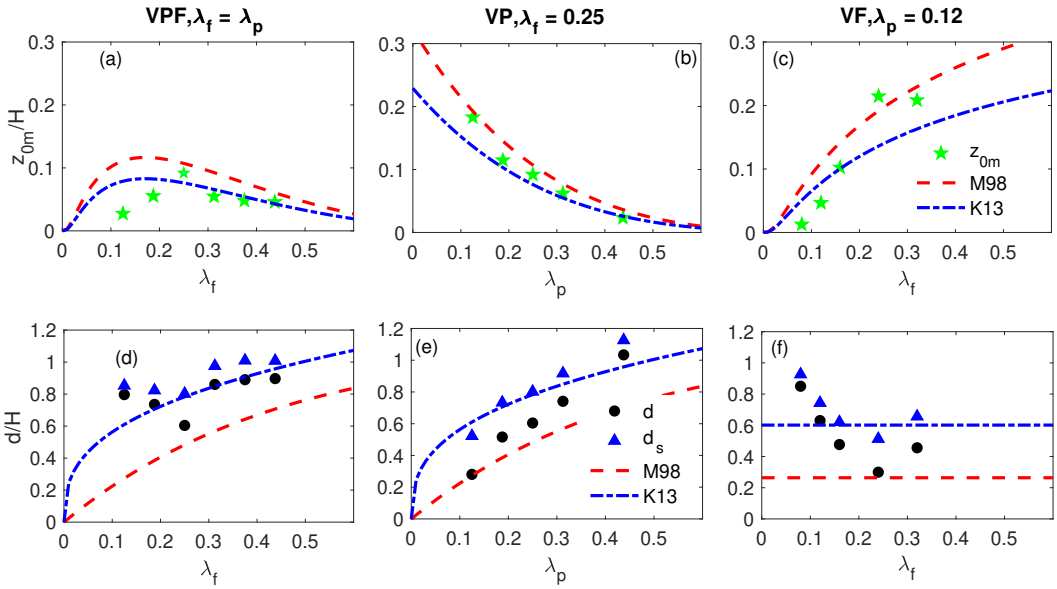

FIGURE 4 Variation of z_{0m} and d determined by direct fitting to LES output for $z/H = 1.25 - 2.25$. (a)-(c):z_{0m} and (d)-(f):d. Macdonald et al. (1998) (red-dotted line) and Kanda et al. (2013) (blue-dash-dotted line) models are also shown for categories: (a,d) VPF; (b,e) VP; (c,f) VF.

One interesting feature of the LES results is the opposing effects of λ_p and λ_f on z_{0m} (Fig. 4b and c) that combine

to explain the non-monotonic behavior in the VPF cases ($\lambda_p = \lambda_f$). Because of the opposing effects, a peak in z_{0m} is expected and occurs between $\lambda_p = \lambda_f = 0.25$ and 0.31 (see Fig. 4a). This peak in z_{0m} has been observed in many previous studies (Kanda et al., 2004; Hagishima et al., 2009; Leonardi and Castro, 2010) for arrays of cubical roughness in which λ_p and λ_f are set equal. Such non-monotonic behavior was also noted by Macdonald et al. (1998) as the obstacles become more densely packed. The peak value of z_{0m}/H is around 0.1 (Fig. 4), which is different from the cubical arrays considered by previous studies (Leonardi and Castro, 2010) reporting the peak value of z_{0m}/H to be around 0.15. This is likely caused by the obstacles in VPF not being cubes with equal dimensions in all directions, except for VPF25.

The variations of z_{0s} (Fig. 5a-c) between different cases overwhelmingly outweigh the effects of changes in z_{0s} when d or d_s are used in the fitting. Values of z_{0s} computed using d differ from those using d_s by less than 10% for more than half of the cases (with a highest deviation of 20%). Such differences do not change the trend of variation across cases and produce negligible change in the values of $\log(z_{0m}/z_{0s})$ (at most 0.3%). Our assumption $d = d_s$ is justifiable for the boundary conditions imposed here. As with z_{0m}, λ_p and λ_f have inverse impacts on z_{0s}, but are exactly opposite to that noted for z_{0m}. The z_{0s} increases with increasing λ_p and decreasing λ_f.

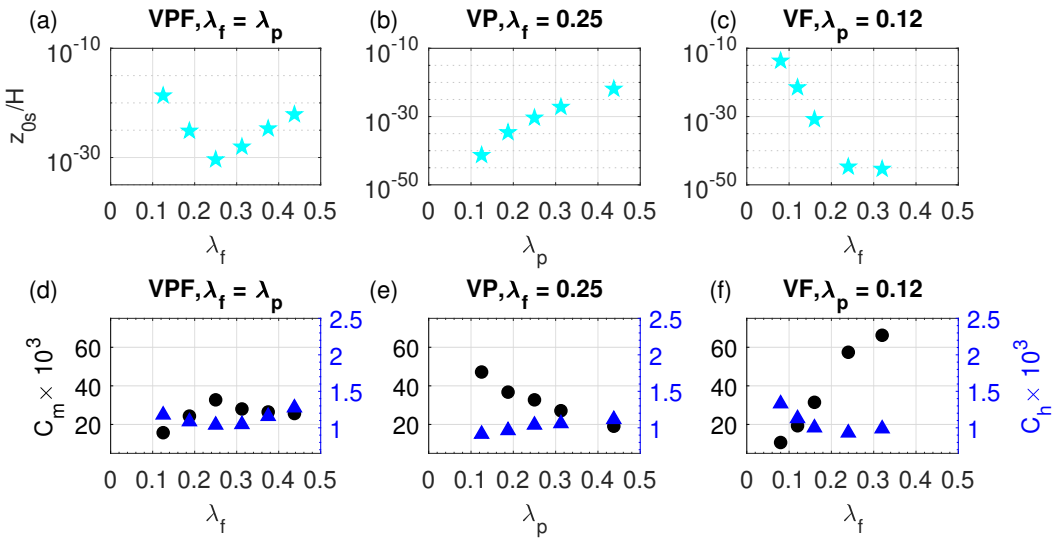

FIGURE 5 (a)-(c): The z_{0s} determined from least-square error minimization using d. (d)-(f): The bulk transfer coefficients for momentum (C_m) and scalar (C_h) computed at z/H =1.5.

The bulk transfer coefficients for momentum and scalar are defined as

$$C_m(z) = \kappa^2 \left(\log\left(\frac{z-d}{z_{0m}} \right) \right)^{-2} \tag{6}$$

and

$$C_h(z) = \kappa^2 \left(\log\left(\frac{z-d}{z_{0m}} \right) \right)^{-1} \left(\log\left(\frac{z-d_s}{z_{0s}} \right) \right)^{-1}, \tag{7}$$

and are shown in Figs. 5d-f for z/H =1.5. The C_m and C_h values are height dependent quantities (sometimes a factor of 2 is used in these definitions). The C_h values obtained here are within the range of scalar transfer coefficients obtained from previous wind-tunnel experiments (Barlow et al., 2004; Chung et al., 2015). A scalar transfer coefficient was derived using two-dimensional street canyon and a naphthalene sublimation technique (Barlow et al., 2004) ranges from 1 $\times 10^{-3}$ to 3.5 $\times 10^{-3}$ (see their figure 4). Likewise, a C_h that ranges between 3 $\times 10^{-3}$ to 3.75 $\times 10^{-3}$ was obtained from measurements of wetted surfaces using three-dimensional arrays of cubes (Chung et al., 2015). While uncertainty in the adopted scalar flux wall-model does affect θ_* and hence C_h, the determined C_h seems to be robust with such uncertainty. The uncertainty from the wall modeling approach to C_h is estimated to be approximately 25% (Li et al., 2016b). The differences might also be related to the lower Re in the wind tunnel experiments. As the relative change in C_h across the cases considered here exceeds 25%, the morphological dependence, at least qualitatively, still holds. The C_m and C_h combine the effects of the displacement height and roughness length on the surface exchange effectiveness, and they show independent monotonic variation with λ_p or λ_f. Their anti-correlated trends with respect to varying geometric parameters confirm that there can be significant "trade-off effects" in the effectiveness of a surface to exchange momentum or scalars with a turbulent flow.

From Eq. 7 the magnitude of z_{0s} can be understood, as C_h depends on both z_{0s} and z_{0m} even with a constant C_h, if the wall gets rougher and both pressure drag and z_{0m} increase, z_{0s} must decrease. Therefore, z_{0s} alone is insufficient to understand wall heat transfer effectiveness (C_h is better for this task). Moreover, the very small magnitudes of z_{0s} do not imply a vanishingly small heat transfer, and z_{0s} should not be interpreted as a macroscopic physical length scale or morphometric parameter. One can note, for example, that the reported values here (and elsewhere) are smaller than the mean free path of atmospheric molecules (i.e. about 70 ηm). This clarifies why determining z_{os} from morphological parameters remains a daunting task for urban canopies and other surfaces as well (at least when compared to z_{om}).

As indicated, z_{0s} is commonly obtained from z_{0s}/z_{0m} or $\kappa B^{-1} = \log(z_{0m}/z_{0s})$ as a function of Re_*. Justified on the grounds that z_{0m} is reasonably described from simplified two-parameter models (e.g. λ_f, λ_p), as confirmed here. For a variety of surfaces, including bluff-rough surfaces, a relation of the form $z_{0s}/z_{0m} \sim Re_*^n$ is used (Brutsaert, 1965, 1975b; Zilitinkevich et al., 2001; Li et al., 2017; Katul and Liu, 2017; Castellví, 2018). A variety of exponents (n=0, 1/4 or 1/2) and intercepts have been reported across differing surfaces. Their universal character is questioned in several studies. The next section discusses such parameterization using a phenomenological model based on surface renewal theory, which has rarely been applied to urban canopies. Its development here constitutes one of the main theoretical novelties of this paper.

4 | SCALAR ROUGHNESS LENGTH FROM SURFACE RENEWAL THEORY

Since Danckwerts (1951) first introduced a statistical model that accounts for duration over which eddies are in contact with an interface (i.e. interval between renewals), extending the surface renewal theory (SRT) to model turbulent transport of scalars in the atmospheric boundary layer has been the subject of inquiry for the past 40 years (Brutsaert, 1975b; Clayson et al., 1996; Katul et al., 1996; Snyder et al., 1996; Denby and Snellen, 2002; Katul et al., 2006; Castellvi et al., 2008; Li et al., 2017). Most applications of the SRT are limited to the "natural" rough and smooth surfaces such as the ocean surface (Clayson et al., 1996), glacier surfaces (Denby and Snellen, 2002), grasslands (Li et al., 2017) and forests (Katul et al., 1996). Whether the surface renewal concept is applicable to *very rough* surfaces that consist of large bluff-body objects such as buildings is now considered within the context of interfacial scalar transfer.

4.1 | Basics of Surface Renewal Theory

The basic assumptions common to all SRT schemes are briefly reviewed. A parcel of air sweeps to the surface and is in contact with the surface for a random duration s. During the interval s, the parcel exchanges mass or heat with the surface via molecular diffusion only. After s, the parcel is ejected and is replaced by a new parcel. In the simplest SRT, this repeated sweep-ejection-replacement process leads to what is labeled as 'continuous surface renewal'. The distributional properties of s, $\phi(s)$ must be externally supplied and are assumed to follow an exponential form (Danckwerts, 1951). Other forms (e.g. log-normal, power-law, Gamma, Inverse-Gaussian) have also been proposed with various justifications (Katul and Liu, 2017). The choice $\phi(s) = R\exp(-Rs)$ is the simplest and most convenient - it defines the probability density function for the rate of occurrence of a surface renewal event and satisfies the normalizing property $\int_0^\infty \phi(s)ds = 1$. This one-parameter probability density function requires only the specification of $1/R$. Physically, $1/R = \int_0^\infty s\phi(s)ds$ is the mean time that an eddy remains in contact with the surface before it is ejected away. In general, $\phi(s)$ must only depend on the flow properties, not the scalar being analyzed. The exact functional form of $\phi(s)$ appears not to be as crucial as the specification of $1/R$ - at least for mean flux calculations as discussed elsewhere (Katul and Liu, 2017). In all SRT versions, the scalar transfer at the surface over a contact duration s is, as earlier noted, assumed to be via molecular transfer characterized by D_m and a local gradient at the surface during event s. To a leading order, this near-surface concentration gradient during s can be approximated by $(\Delta\theta')/\sqrt{D_m s}$, where $\Delta\theta'$ is assumed to be primarily dominated by mean scalar changes within the local interfacial layer with a characteristic thickness $\sqrt{D_m s}$ (the layer bounded by red dotted line in Fig. 1b; i.e. at the micro-scale and accommodated only in the wall model of the LES).

With the choice of the distribution function $\phi(s) = R\exp(-Rs)$, the mean thickness of the local interfacial layer is L_i given by

$$L_i \propto \int_0^\infty \phi(s)(D_m s)^{1/2} ds = \frac{1}{2}\sqrt{\frac{\pi D_m}{R}}. \tag{8}$$

Mean temperature changes from L_i to any height above L_i are assumed to be minor when compared to $\Delta\theta'$ within L_i. This is required in SRT because differences in temperatures of air parcels originating from outside this interfacial layer are not explicitly considered, and $\Delta\theta'$ is thus strictly controlled by the surface flux. With this background, the heat flux summed over all random contact times must be given as

$$F_c = -\int_0^\infty \phi(s) D_m \left(\frac{\partial\theta}{\partial z}\right)_{z=0} ds \propto -D_m \int_0^\infty R\exp(-Rs)\frac{\Delta\theta'}{(D_m s)^{1/2}} ds. \tag{9}$$

This expression can be arranged to yield

$$Sh = \frac{F_c}{u_*\Delta\theta'} = \frac{1}{u_*} A\pi {D_m}^{1/2} R^{1/2}, \tag{10}$$

where Sh is the Sherwood number (a type of a mass transfer Stanton number) and A is a proportionality constant. When the total scalar or heat fluxes and u_* are constant with z and the primary $\Delta\theta'$ is across the interface, the Sh can be interpreted as both an interfacial and a bulk (i.e. extending to the inertial layer, not just the interfacial layer) characteristic. These assumptions are common to virtually all SRT. The main difference between various SRT approaches is broadly in how $1/R$ is specified. It is thus instructive to analyse these approaches using two 'end-member' cases: the micro-eddy and macro-eddy models (Fig. 6) characterizing $1/R$.

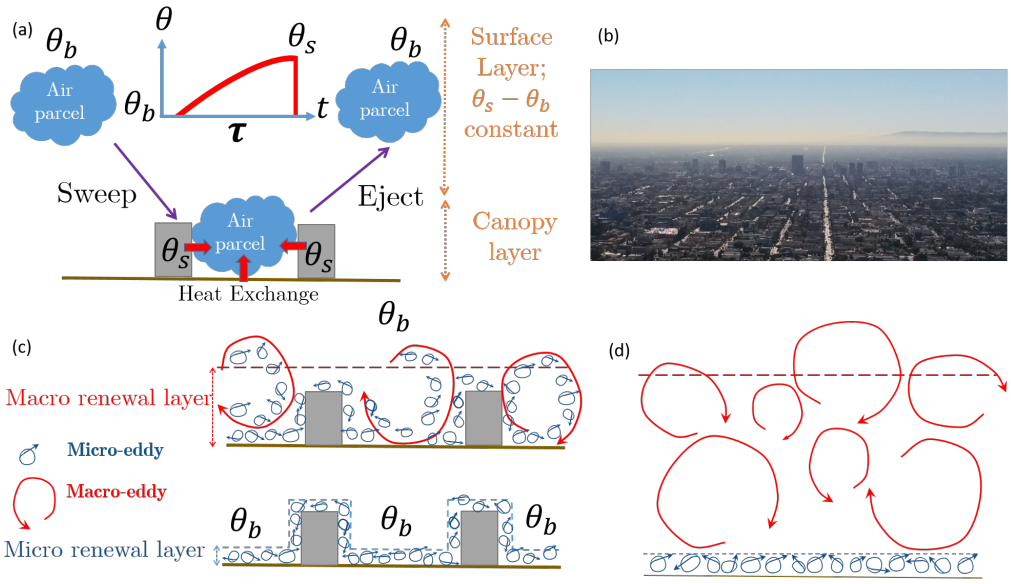

FIGURE 6 A schematic illustrating the (a) continuous surface renewal theory (SRT) process and (b) a typical urban bluff-rough surface. (c) concepts of the micro-scale and macro-scale eddies viewed in the context of SRT, and (c) with bluff bodies and (d) without bluff bodies. For the micro-eddy model, it is assumed that the limiting step in the scalar exchange process is availability of Kolmogorov eddies that can populate the entire surface area. For the macro-eddy model, the ability to produce or bring Kolmogorov eddies to the exchanging surface by macro-eddies is considered to be the limiting step.

4.2 | The micro-eddy model

In the micro-eddy model, it is assumed that large eddies can be efficient in bringing air parcels (and small eddies) near the solid interface but do not interact with the interface. Heat or mass exchange at the solid interface must only occur after air parcels penetrate and momentarily break-up the viscous sublayer and make direct contact with the solid surface. Hence, we take the view that only the smallest of eddies (active in the viscous and buffer layers) are sufficiently efficient at penetrating the viscous sublayer to interact with the surface. According to the micro-eddy model, this efficiency is not based on the energy content of an eddy. If an eddy is sufficiently energetic to penetrate into or displace the viscous sublayer, any excess kinetic energy carried by the eddy is not used in the renewal and its interaction with the surface will not depend on this excess. Hence, the micro-eddy model assumes that it is the collision frequency between eddies and the viscous sublayer that dictates the renewal frequency, not the energy content of eddies. Very small eddies in the vicinity of the interface are expected to experience collision events with the viscous sublayer at a high frequency when compared to large eddies. Because of the high frequency of collisions, the very small eddies encounter the viscous sublayer far more frequently (at least compared to their much larger eddies counterparts) and contribute to scalar mass exchange. In the energy cascade, these small eddies are commensurate in size with the so-called Kolmogorov viscous length scale (Brutsaert, 1965). Under such a condition, $1/R$ is assumed to scale with the Kolmogorov time scale $= (\nu/\epsilon)^{1/2}$, where ϵ is the mean turbulent kinetic energy dissipation near the interface. With $R = (\nu/\epsilon)^{-1/2}$ (flow and fluid properties) and $D_m = Sc^{-1}\nu$,

$$Sh = \frac{F_c}{u_*\Delta\theta'} = \frac{1}{u_*}A(\pi Sc^{-1})^{1/2}(\nu\epsilon)^{1/4}, \tag{11}$$

where $(\nu\epsilon)^{1/4}$ is the Kolmogorov velocity with an associated kinetic energy $= (\nu\epsilon)^{1/2}$.

This micro-eddy model thus postulates that the canyon sublayer air in between the buildings has comparable scalar concentration to the roughness and inertial layer air, and that the micro eddies then sweep this canopy layer air in contact with various facets where it is further enriched in scalar concentrations. To place this result in the context of prior theories (Brutsaert, 1965), the following representation of the cuboid surface can also be made. The cuboids-air interface is first replaced by an equivalent rough surface (i.e. experiencing the same scalar flux and u_*) characterized by z_{0m} and positioned at $z = d$ (Fig. 1c thick brown line). For this rough surface, the turbulent kinetic energy dissipation rate inside the equivalent roughness elements (characterized by z_{0m}) is assumed to be given by the balancing mechanical production term (i.e. assuming local equilibrium)

$$\epsilon = u_*^2\frac{du}{dz} \propto u_*^2\frac{u_*}{\kappa z_{0m}}. \tag{12}$$

For these assumptions, it directly follows that

$$Sh = A'Sc^{-1/2}(Re_*)^{-1/4}, \tag{13}$$

where A' is another similarity constant. Hence, the micro-eddy model (Brutsaert, 1965) predicts a $Sh \propto Re_*^{-1/4}$. For most trace gases (or temperature), Sc (or the Prandtl number Pr) is near unity in air and plays a lesser role (it was assumed unity in the LES here). Another important feature of the micro-eddy model is that the resulting $L_i \propto Sc^{-1/2}\eta$ (i.e. the Batchelor length), where $\eta = (\nu^3/\epsilon)$ is, as before, equal to the Kolmogorov length scale. This scale is not resolved in the LES but is represented by the wall model.

4.3 | The macro-eddy model

In this representation, the limiting step to heat or scalar exchange is assumed to be the efficiency of large coherent eddies to deliver parcels of air to the surface that then enable Kolmogorov eddies to exchange heat with the interface. The canopy sublayer air has a significantly higher concentration than the roughness sublayer air aloft, and surface renewal requires a large eddy to penetrate into, and ventilate, the canopy layer to sustain surface fluxes. Previous studies over large bluff-body obstacles (Leonardi et al., 2015) demonstrated that organized eddy motions indeed dominate in the roughness and canopy sublayers for turbulent scalar transport. For 'obstructed shear flows' (Ghisalberti, 2009) such as flows over urban canopies, the canopy flow can be characterized by the penetration depth (L_s) of the vortices into the canopy sublayer. These can be linked to the shear length scale defined as $L_s = \frac{\overline{u}}{d\overline{u}/dz}$ for $z = H$ at the mean canopy height (Raupach et al., 1996). For most canopies, except the sparse ones, $L_s \leq H$ and in general L_s is of the order of H (Raupach et al., 1996; Katul et al., 1998; Poggi et al., 2004; Li and Bou-Zeid, 2019). The characteristic mean contact time scale can be related to the mean vorticity time scale, $(d\overline{u}/dz)^{-1}$ at $z = H$, which is L_s/U_H, where $U_H = \overline{u}(z = H)$. In addition, if the log-profile is extrapolated to $z = H$, $d\overline{u}/dz \approx u_*/(\kappa z_{0m})$. Indeed, the LES results depicted in Fig. 7a confirm that $(d\overline{u}/dz)^{-1} = L_s/U_H$ is correlated with u_*/z_{0m} (correlation coefficient is 0.73 with a p-value = 0.001). For this macro-eddy model, the characteristic mean contact time of renewal is proportional to the mean vorticity time scale (instead of the Kolmogorov time scale). Conceptually, this assumption implies that each single large coherent eddy leads to a single renewal event of the canopy sublayer air, and the number of renewal events must be identical to the frequency of occurrence of coherent events. Meanwhile, numerous other turbulent events, including Kolmogorov-sized eddies, renew the viscous sublayer multiple times but they are not the bottleneck in the renewal process (as their generation and delivery is dependent on the macro-eddy). This physical picture implies that large canopy-layer air ventilation events control the renewal rate, and that the entire building facet area then exchanges heat or scalars with each coherent eddy. Stated differently, the renewal eddy is 'space-filling' over a large contact area in this macro-eddy model. One can then contrast this to the micro-eddy model where numerous Kolmogorov eddies are assumed to be present at all points in the flow domain including all points around building facets.

Mindful of these physical assumptions, this macro-eddy model leads to

$$\frac{1}{R} \sim \frac{L_s}{U_H} \sim \kappa \frac{z_{0m}}{u_*}. \tag{14}$$

Now that the rate of surface renewal from macro eddies is estimated, it directly follows from Eq. 10 that

$$Sh = A'' Sc^{-1/2} Re_*^{-1/2}. \tag{15}$$

Therefore, the differing assumptions between the micro- and macro-eddy models result in distinct scaling laws between Sh and Re_*.

4.4 | The chain-saw model

This model was originally formulated to explore air-water gas exchange in streams (Moog and Jirka, 1999). The basic assumptions can be contrasted to the urban roughness exchange mechanisms discussed here. In its original form, surface renewal is analogous to a chain-saw cutting a tree. The small teeth of the chain-saw perform the actual cutting (much like the Kolmogorov eddies cutting through the viscous sublayer in the micro-eddy approach) but the

chain speed and the larger saw blade (much like the large and coherent eddies) carry the small-teeth to the cutting zone (the viscous sublayer attached to solid boundaries). Both the speed of the chain and the access of the small blades to the cutting zone control the actual cutting. Both scales 'cooperate' and can now be incorporated for urban roughness by adopting the active zones approach of the chain saw model. In this case, each eddy penetration encounters an incomplete interfacial area not covering the entire surface area. The chain-saw model then assumes that within each patch area covered by the big eddy, Kolmogorov (or Batchelor) sized eddies carry out the scalar exchange as in the micro-eddy model. The micro-eddy model still represent the correct physics but must be amended to include the 'active zone' fractional area A_a^+ reflecting the penetration and renewal from large eddies. It is straightforward to show that this representation leads to

$$Sh = A' Sc^{-1/2} (A_a^+) (Re_*)^{-1/4}, \tag{16}$$

where A_a^+ is now expected to scale with Re_* and the arrangement of the roughness elements. If $A_a^+ \sim Re_*^0$, then the micro-eddy model is restored, whereas with $A_a^+ \sim Re_*^{-1/4}$, the macro-eddy model is recovered.

In the chain-saw model, at a fixed Sh and for an imposed u_* dictating the energy available for eddy penetration into the canopy elements (set by u_*^2), increasing z_{0m} increases Re_* but reduces the eddy penetration and hence A_a^+. The chain-saw model is featured here not because of its prognostic skills - but its diagnostic skills. It suggests that a number of possible exponents are possible depending on how efficient the eddy penetration into the cuboids is. Another amendment to the chain-saw model may include the spatial intermittency of ϵ at the walls of the cuboids for each eddy penetration, adding another relation between Re_* and ϵ. The scaling of A_a^+ with Re_* is rarely studied in urban canopies and must be externally supplied for now. Nonetheless, the analysis here provides plausible explanations as to why differing scaling exponents for $Sc - Re_*$ may have been reported in the literature.

4.5 | Linking Surface Renewal to κB^{-1}

As noted, the Sh derived from SRT can be interpreted as both an interfacial and bulk characteristic extending to the inertial layer. If so, Sh can then be determined from equation 2 in the neutral limit as

$$Sh^{-1} = \frac{1}{\kappa} \log\left(\frac{z - d_s}{z_{0s}}\right). \tag{17}$$

Similarly, the interfacial bulk drag coefficient for the virtual bluff-rough surface C_m, Eq. 6, can be related to z_{0m} as

$$C_m^{-1/2} = \frac{1}{\kappa} \log\left(\frac{z - d}{z_{0m}}\right). \tag{18}$$

Then, assuming $d = d_s$, z_{0m} and z_{0s} can be related using Sh and C_m using

$$z_{0s} = z_{0m} \exp\left[-\kappa\left(Sh^{-1} - C_m^{-1/2}\right)\right], \tag{19}$$

in which $Sh^{-1} - C_m^{-1/2}$ is usually referred to as B^{-1}, i.e. $z_{0s} = z_{0m} \exp\left[-\kappa B^{-1}\right]$. For the macro-eddy model, the B^{-1} can be expressed as:

$$B^{-1} = Sh^{-1} - C_m^{-1/2} = A_1 Re_*^{1/2} - C_m^{-1/2} = A_1 Re_*^{1/2} + A_2, \tag{20}$$

where A_1 is $1/A'$, and $A_2 = -C_m^{-1/2}$. In the fully rough limit at high Re, C_m only depends on the geometry of the surface and should become Reynolds-number independent (equivalent to stating that d and z_{0m} are independent of wind speed and fluid viscosity). It is also worth noting that the A_2 parameter obtained as the intercept from field data using statistical regression (Kanda et al., 2007) has a clear physical meaning that pertains to the bulk drag coefficient as $A_2 = -C_m^{-1/2}$, and it is constant only under the assumption of C_m being a much weaker function of Re_* than Sh.

Fig. 7a shows the calculated B^{-1} from LES for all the three-dimensional rough surfaces in Table 1; models from Brutsaert (1965, 1975a) and Kanda et al. (2007) are also shown. The model by Brutsaert (1965, 1975a) is based on the micro-eddy model and results in $B^{-1} = C_1 Re_*^{1/4} + C_2$ instead of $Re_*^{1/2}$ for the macro-eddy model. The model by Kanda et al. (2007) assumes the same one-fourth power relation between B^{-1} and Re_*. These models with an exponent $\approx 1/4$ do not seem to be the most appropriate for the large bluff roughness elements of this study despite the fact that they were reported to match observations better (than ones with exponents $\approx 1/2$) over natural surfaces such as waves (Li et al., 2018). We could improve these models by refitting their constants to the LES data, but given the mismatch in the slope this was deemed unnecessary. The macro-eddy model captures the LES derived B^{-1} - Re_* scaling better. Additional relevant models in the literature are shown in Table 2. Zilitinkevich et al. (2001) obtained $Re_*^{1/2}$ scaling, but the result was derived based on dimensional analysis without invoking surface renewal theory (yet it matches the macro-eddy model in scaling).

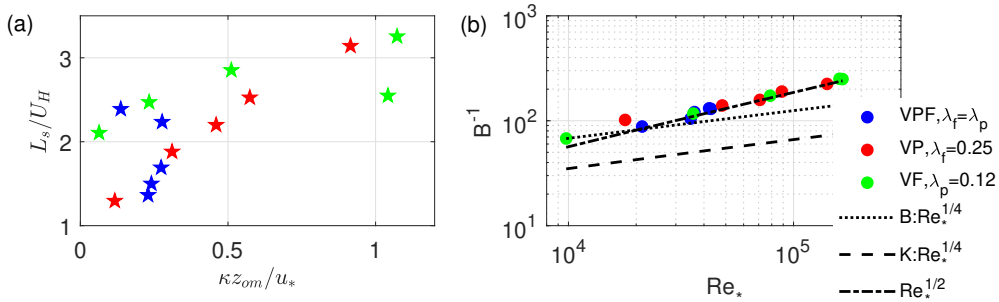

FIGURE 7 (a) The relation between L_s/U_H and $\kappa z_{0m}/u_*$ showing reasonably-linear trends. The macro-eddy model assumes that the mean contact time $1/R$ can be estimated as $\kappa z_{0m}/u_*$. (b) B^{-1} as a function of $Re_* = u_* z_{0m}/\nu$ from LES and various models. The SRT predictions from the micro-eddy and macro-eddy models are also shown.
B:$Re_*^{1/4}$ Brutsaert (1975b) model: $7.3Sc^{1/2}Re_*^{1/4} - 5$.
K:$Re_*^{1/4}$ Kanda et al. (2007) model: $6.4Re_*^{1/4} - 5$.
$Re_*^{1/2}$ least-square regression of the macro-eddy power law model: $B^{-1} = Sh^{-1} - C_m^{-1/2}$=$0.60Re_*^{1/2} - 3.5$.

A least-square regression with $Re_*^{1/2}$ yields the constants $A_1 = 0.68$ and $A_2 = 3.5$ (Table 2, Method 1). Least-square fitting of $Sh^{-1} \propto Re_*^{1/2}$ and $Sh^{-1} \propto Re_*^{1/4}$ found that the 1/2 scaling yielded a coefficient of determination of 0.96 (cf. 0.80 for the 1/4 scaling). This finding confirms that the SRT with the macro-eddy representation is consistent with the wall-modeled LES computations of macro-scale scalar roughness length. It should also be noted that B^{-1} versus Re_* can have a large range of variability (cf. Figure 6 in Kanda et al. (2007), Figure 2 in Crawford et al. (2018)), which can be attributed to variability in the multiplicative factor A_1 or from other physical processes not captured here that could also alter the power exponent relating B^{-1} and Re_*.

The functional dependence between Sh^{-1} and Re_* (Fig. 8) can now be exploited to propose a new approach to parameterize z_{0s} for urban terrain. Morphometric models, (e.g. Kanda et al. (2013) can be used to obtain z_{0m} and d, and therefore compute $C_m^{-1/2}$, according to Eq. 18 for a given z). Using Eq. 20 with $A_1 = 0.70$ deduced from LES

here, (or fit other observational or LES data for other distinct geometries), z_{0s} results are obtained (Table 2, Method 2). Direct evaluation of z_{0s} obtained from LES in Fig.8b (we compare the logarithms since they are the forms that appear in conventional models) have good agreement.

Reference	B^{-1}
Owen and Thomson (1963)	$2.40Re_*^{0.45}$
Brutsaert (1975a)	$7.3Sc^{1/2}Re_*^{1/4} - 5$
Cahill et al. (1997)	$4.31Re_*^{1/4} - 5$
Zilitinkevich et al. (2001)	$0.5Re_*^{1/2} - 3.2$
Method 1: Eq. 20 with constant A2	$0.60Re_*^{1/2} - 3.5$
Method 2: Eq. 20 with variable $A_2 = -C_m^{-1/2}$ from morphometric model	$0.70Re_*^{1/2} - C_m^{-1/2}$

TABLE 2 Relation between B^{-1} and roughness Reynolds number Re_* from different studies.

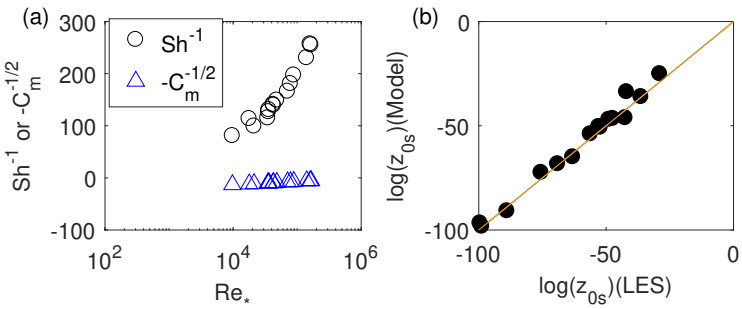

FIGURE 8 Variations of Sh^{-1} and $C_m^{-1/2}$ with Re_* (a) and scalar roughness length z_{0s} modelled (Method 2, Table 2) versus results directly from LES.

5 | CONCLUSIONS

Large-eddy simulations for urban surfaces consisting of arrays of large cuboids are conducted to address how urban roughness elements impact the variations of scalar roughness length when compared to its momentum counterpart. The simulations had frontal area density λ_f and plan area density λ_p varied independently. The variations in z_{0m} are linked to the combination of increasing with λ_f and decreasing with λ_p. Models based on morphometric parameters have acceptable predictive power to capture these trends for z_{0m}. To link such models for z_{0m} to z_{0s}, the $\kappa B^{-1} = \log(z_{0m}/z_{0s}) = A_1 Re_*^n + A_2$ framework was used. An approach based on the surface renewal theory is proposed to determine n. The exponent derived here closely follows its theoretical prediction when the mean contact time is derived from macro-eddy properties ($n = 1/2$) instead of micro-eddy properties ($n = 1/4$). An alternative model that is based on the chain-saw analogy was also explored. This model features an effective contact area depending on eddy penetration, and can recover either the micro- or macro-eddy models scaling, depending on how this area scales with

Re_*.

The results here have three major implications:

(i) There are "trade-off effects" in the effectiveness of a very-rough surface in exchanging momentum and scalars with a turbulent flow as can be deduced from the opposing trends of C_m and C_h with changes in geometry. Similar findings have been reported over steep waves (Sullivan et al., 2017). These findings illustrate the contrasting effects of roughness elements, as discussed by Brutsaert (1975b) and others: "... (roughness elements) on the one hand, they act as windbreaks, reducing surface exposure and thus transfer, while on the other hand, they increase drag and thus shear with a concomitant increase in eddy diffusivity". Roughness elements are usually applied to a smooth wall to increase turbulence mixing, which enhances both drag and heat transfer. For urban surfaces, the results here imply that as the density of roughness elements increases, a point will be reached beyond which convective heat transfer will become less efficient. Similarly, skin hairs promote heat transfer at low densities but acts as insulators at higher densities (Fowler and Bejan, 1995).

(ii) In contrast to land surface models that postulate a relation $z_{0s} \propto z_{0m}$ (usually with a pre-factor of 1/10), the LES predicts that an increase in z_{0m} results in a decrease z_{0s}. In addition, the macro-eddy SRT model proposed in this paper, as well as all other models evaluated here (including those closely following the micro-eddy SRT) also predict an inverse relation of the two roughness lengths (for typical values of the friction velocity, air viscosity and momentum roughness length in urban terrain; Fig. 9a with a friction velocity u_*= 1 m s^{-1}). Different values u_* values dictate changes in z_{0s} as z_{0m} varies, which gives rise to the scatter in LES results shown in Fig. 9b. Data from other studies are also shown in Fig.9b. Despite the large range of uncertainty, that z_{0s} decreases with increasing z_{0m} is consistent with these data.

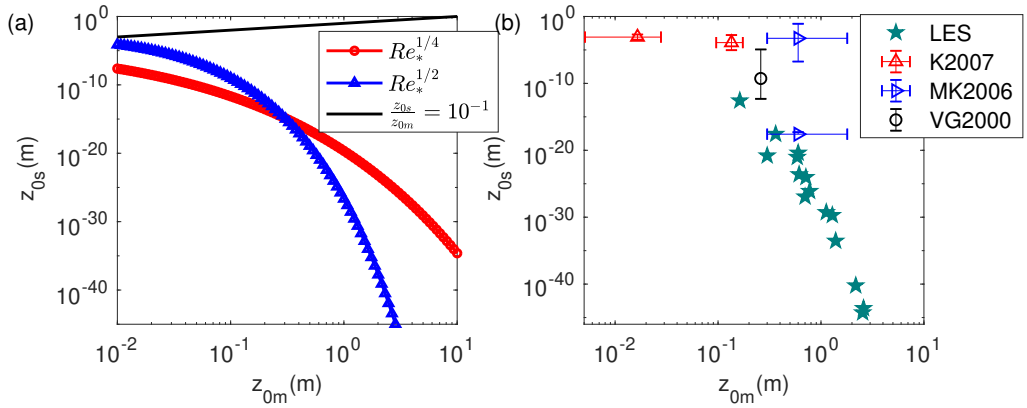

FIGURE 9 (a): Variation of z_{0s} with z_{0m} for a typical friction velocity u_* =1 m/s, ν=1.46×10^{-5} m^2/s. z_{0s} modeled with Brutsaert (1975a) (red circle); z_{0s} modeled with Method 1 in this study (blue triangle); z_{0s}/z_{0m}=10^{-3} (black line). (b): LES and previous field measurements. LES (teal stars); K2007 (red triangle): outdoor urban scale models in Kanda et al. (2007), the whiskers indicate standard deviations of momentum and heat roughness lengths reported in Table 3 of Kanda et al. (2007); MK2006 (blue triangle): measurements from a suburban site in Tokyo, Japan by Moriwaki and Kanda (2006b) showing momentum, heat (upper triangle) and water vapor (lower triangle) roughness lengths reported in Table 1 of Moriwaki and Kanda (2006b), where the whiskers indicate their respective standard deviations; VG2000 (black circle): measurements from a light industrial site in Vancouver, British Columbia, Canada from (Voogt and Grimmond, 2000). Data are extracted from their Fig.8a, where the whiskers indicate the range of heat roughness lengths.

(iii) As obstacle-resolving LES is becoming a promising tool to explore urban atmospheric boundary layers. However, how to interpret the bulk transfer properties directly computed from LES, especially for scalars, remains a subject of inquiry. The values that emerge from the analysis can depend on the wall-model used to link the obstacle surface to the flow. The wall-model formulation used here is self-consistent with expected theoretical behavior of an aerodynamically smooth wall, as well as the micro-eddies in the surface renewal theory (Appendix B).

(iv) The feasibility of estimating z_{0s} for urban surfaces using a two-step approach is demonstrated. This should be verified, using field observations and/or LES or DNS, for other more realistic geometries. This method utilizes the Re_* dependence of scalar transfer and the adequate skill of the existing morphometric momentum roughness length models. Here only Macdonald et al. (1998) is used to illustrate this two-step approach to compute C_m. Future studies could use newer models (e.g. (Kanda et al., 2013; Yang et al., 2016; Zhu and Anderson, 2018), etc.) for d and z_{0m} to further refine C_m.

Although the number of cases with idealized cuboids is limited, the generalized framework of both micro- and macro-scale roughness lengths can be extended and tested for other configurations (e.g. a larger morphometric parameter space and realistic urban geometries). In addition, the impact of different thermal boundary conditions and atmospheric stability regimes have been purposely omitted, but these effects are expected to have a significant influence on d, z_{0m}, and z_{0s}. Last, the 'chain-saw' model for surface renewal opened up the inquiry into how to connect the penetration of eddies into the roughness elements with Re_* and whether the turbulent kinetic energy dissipation rate is spatially intermittent with patchy contact wall areas that scale with Re_*. Recent advances in thermal infrared imaging may offer some clues on how to proceed; this is also a topic that can be explored using DNS in future studies.

Appendix A: Numerical setup

The LES model used here implements the immersed boundary method (IBM) to resolve the bluff-body obstacles explicitly. The non-dimensional filtered incompressible continuity (A 1), Navier-Stokes (A 2) and scalar conservation (A 3) equations are solved assuming hydrostatic equilibrium of the mean flow:

$$\frac{\partial u_i}{\partial x_i} = 0, \tag{A 1}$$

$$\frac{\partial u_i}{\partial t} + u_j \left(\frac{\partial u_i}{\partial x_j} - \frac{\partial u_j}{\partial x_i} \right) = -\frac{\partial p}{\partial x_i} - \frac{\partial \tau_{ij}}{\partial x_j} + F_i + B_i, \tag{A 2}$$

$$\frac{\partial \theta}{\partial t} + u_i \frac{\partial \theta}{\partial x_i} = -\frac{\partial q_i^s}{\partial x_i}, \tag{A 3}$$

where x, y and z denote the streamwise, cross-stream and wall-normal directions respectively, and u, v and w are the velocity components in these respective directions; t denotes time; u_i is the resolved velocity vector; p is the modified pressure; τ_{ij} is the deviatoric part of the subgrid stress tensor; F_i is the body force driving the flow (here simply a homogeneous steady horizontal pressure gradient imposed along the x direction); and B_i is the immersed boundary force representing the action of the obstacles on the fluid. In equation (A 3), θ denotes the concentration of a passive scalar quantity and q_i^s is the i^{th} component of the subgrid scale scalar flux. All the variables used are the filtered components, although the usual tilde on top is omitted for notational simplicity. Equations A 1 to A 3 are pre-normalized by the friction velocity that accounts for the total (viscous and form) surface drag (u_*), the boundary-layer depth (δ), air density (ρ) and a reference scalar quantity (θ_0).

The passive scalar θ considered here is temperature, but the buoyancy force is omitted to mimic a passive scalar (the gravitational acceleration is set to zero); the results would be applicable to all other nearly-passive scalars such as water vapor. However, future extension to include buoyant forces under strong heating is required to proceed towards realistic conditions. An isothermal boundary condition of 330K is imposed on all surfaces. Horizontal periodic boundary conditions are applied to all quantities. The top boundary conditions are zero stress and scalar flux and no-penetration (zero normal velocity). Further details regarding the numerical procedures are described elsewhere (Chester et al., 2007; Li et al., 2016a) and the subgrid scale model is discussed in Bou-Zeid et al. (2005). The code has been verified (Li et al., 2016a,b) for its performance in simulating both momentum- and scalar- transport. All simulations are run for 50 eddy turn-over times defined as δ/u_* and the last 25 are averaged for the statistics analyzed here.

Appendix B: The relation between wall-modeled F_s and z_{0s}^{mic}

Implications of micro-scale roughness values in the LES wall-model in terms of F_s (the scalar fluxes computed from the wall model) are considered. The surface renewal theory (Brutsaert, 1982) for surfaces that are aerodynamically smooth or having intermediate roughness elements indicate a sub-linear dependence on friction velocity ($\propto u_*^{3/4}$) of surface fluxes of passive admixtures. Such a sub-linear dependence discussed elsewhere (Katul and Liu, 2017) has been shown not to depend on the assumptions intrinsic to surface renewal theory. For example, the mean flux of a passive scalar admixture (e.g. water vapor) (Katul and Liu, 2017) is :

$$F_s \propto D_m^{1/2} u_*^{3/4} (\kappa \nu z_{0m}^{mic})^{-1/4} (\theta_s - \theta_h), \tag{B 1}$$

where D_m is molecular diffusivity of water vapor; θ_s and θ_h are mean scalar concentration (or temperature) at the surface and interfacial sublayer, respectively. Physically, the micro-scale roughness length is a bulk representation of the thickness of the interfacial sublayer and of (i) either the molecular processes therein for smooth walls, or (ii) of the roughness geometries of the surface for intermediate rough walls. In the context of the LES with smooth walls here, z_{0m}^{mic} is given by the wall-model (Eq. 3) and also depends on u_*. If we substitute the wall-model into equation B 1, the resulting wall-modeled scalar flux F_s follows

$$F_s \propto \left(\frac{9}{\kappa}\right)^{1/4} Sc^{-1/2} u_*^{wm} (\theta_s - \theta_h), \tag{B 2}$$

where $Sc = \nu/D_m$ is the molecular Schmidt number; θ_h is the mean scalar magnitude in the vicinity of the surface.

By virtue of the wall model here, where Sc=1, Eq. B 2 becomes

$$F_s \propto u_*^{wm} (\theta_s - \theta_h). \tag{B 3}$$

Figure B 1 shows F_s versus u_*^{wm} and the least-square regression using u_*^{wm} computed from all facets for all cases in Table 1. The data from LES suggest that F_s practically follows a linear scaling with u_*^{wm}, (i.e. the power exponent is 1.005 $\approx$ 1.0), which confirms that imposing a smooth-surface micro-scale roughness length in the wall model for LES is consistent with the prediction in Eq. B 3 and the general surface renewal theory scaling when a smooth-wall roughness length is desired. In fact, Eq. B 3 or Eq. 11 are more generalizable results since surface renewal theory at the micro-scale does not need to be invoked to obtain these relations (Katul and Liu, 2017). Imposing a wall function in LES based on the log-law formulation implicitly satisfies the assumptions of Kolmolgorov's inertial subrange scaling

(Gioia et al., 2010). This finding suggests that the results obtained from LES wall-models are not dependent on the validity of surface renewal theory at the micro-scale. The analysis here is intended to show self-consistency of the wall-modeling approach adopted here.

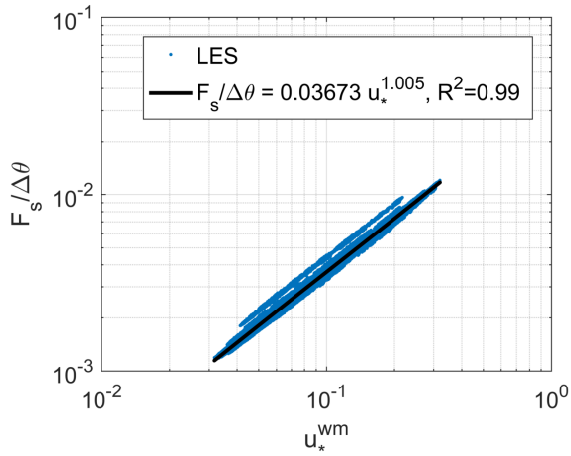

FIGURE B 1 $F_s/(\theta_s - \theta_h)$ versus u_*^{wm} for all LES runs. Each data point represents the mean F_s and u_*^{wm} obtained from the wall model.

Appendix C: Uncertainty Analysis in the Delineation of the Log-Region on Macro-Roughness Parameters

The delineation of the logarithmic region affects the zero-plane displacement and roughness length estimation is explored using least-squares regression fitting over all plausible ranges in the logarithmic region (from just above the building height to three times the building height by visual inspection of the profiles), using at least six points. A relative sensitivity factor is defined for each fitted parameter Y as $Y - Y_0/(Y_{max} - Y_{min})$, where Y_0 is the value for the range of fitting adopted in the paper (i.e. logarithmic region starts from $1.25H$ and ends at $2.25H$); Y is the value of a given range; $Y_{max(min)}$ is the maximum (minimum) value of Y obtained for all possible ranges. The parameters tested are z_{0m}, z_{0s} or d, and their sensitivity plots are shown in Fig.C 1, Fig.C 2 and Fig. C 3, respectively.

The relative sensitivity factor, D_v, averaged for each geometry over all plausible ranges of the log-region in which the least-square fitting is performed, is always less than about 40%, and it is within 20% for most of the cases (Fig. C 4). Therefore, the sensitivity of results to the precise delineation of the logarithmic regions does not change the overall trends in $B^{-1} = \log(z_{0m}/z_{0s})$ as shown in Fig. C 5). The conclusions of the paper are deemed robust to uncertainties in the identification of the log-region.

references

Anderson, W. (2013) Passive scalar roughness lengths for atmospheric boundary layer flow over complex, fractal topographies. *Environmental Fluid Mechanics*, **13**, 479–501.

Barlow, J. F. and Coceal, O. (2009) A review of urban roughness sublayer turbulence. *Met Office Research and Development–Technical Report*, **1**, 527.

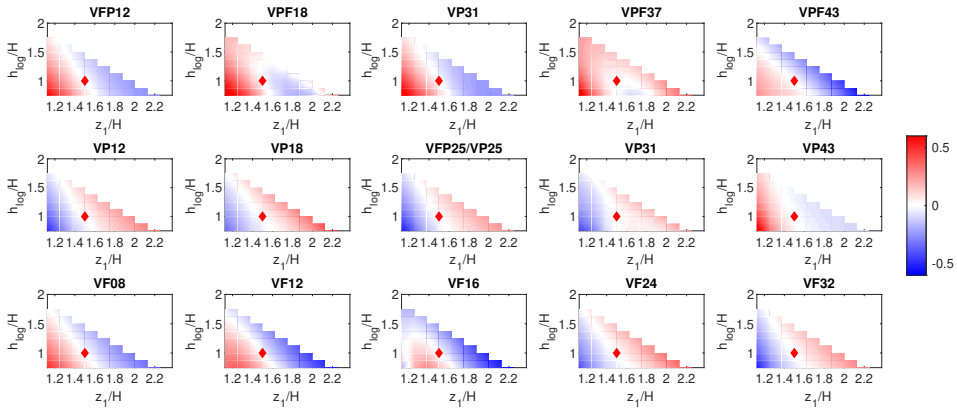

FIGURE C 1 The range of variability of z_{0m} obtained by varying z_1/H, the position where the log-layer commences, and the span of the log-region, h_{log}/H. The red diamond shape denotes the chosen range of the log-region for least-square regression featured in the main text (i.e. $z_1/H = 1.25$ and $h_{log}/H = 1$). Colorbar indicates the relative sensitivity factor.

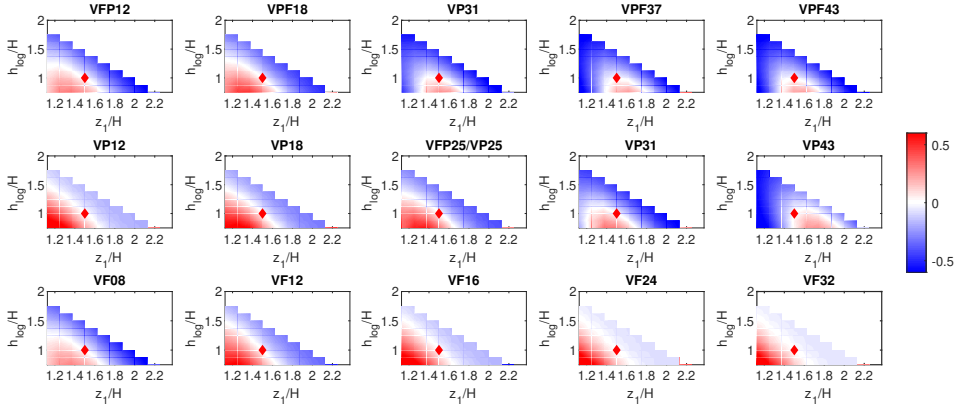

FIGURE C 2 As Fig.C1 , but for z_{0s}.

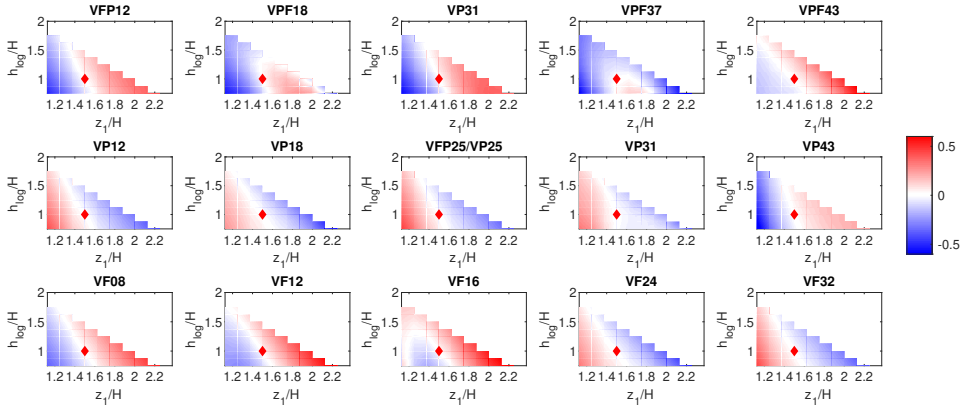

FIGURE C 3 As Fig.C1, but for d.

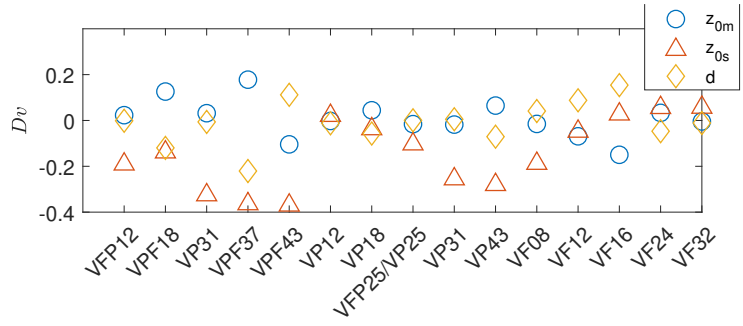

FIGURE C 4 Averaged sensitivity factor Dv for z_{0m}, z_{0s} and d.

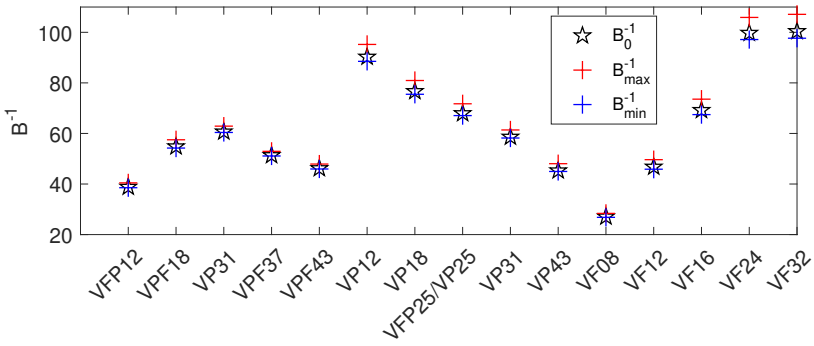

FIGURE C 5 Variation of B^{-1} across cases. B_0^{-1} is computed from z_{0m} and z_{0s} obtained for $z_1/H = 1.25$ and $h_{log}/H = 1$; B_{max}^{-1} and B_{min}^{-1} are obtained from the maximum and minimum values of z_{0m}/z_{0s} for all values from the possible ranges of logarithmic region.

Barlow, J. F., Harman, I. N. and Belcher, S. E. (2004) Scalar fluxes from urban street canyons. Part I: Laboratory simulation. *Boundary-Layer Meteorology*, **113**, 369–385.

Bose, S. T. and Park, G. I. (2018) Wall-modeled large-eddy simulation for complex turbulent flows. *Annual Review of Fluid Mechanics*, **50**, 535–561.

Bou-Zeid, E., Meneveau, C. and Parlange, M. (2005) A scale-dependent Lagrangian dynamic model for large eddy simulation of complex turbulent flows. *Physics of Fluids*, **17**, 1–18.

Bou-Zeid, E., Overney, J., Rogers, B. D. and Parlange, M. B. (2009) The effects of building representation and clustering in large-eddy simulations of flows in urban canopies. *Boundary-Layer Meteorology*, **132**, 415–436.

Brutsaert, W. (1965) A model for evaporation as a molecular diffusion process into a turbulent atmosphere. *Journal of Geophysical Research*, **70**, 5017.

— (1975a) A theory for local evaporation (or heat transfer) from rough and smooth surfaces at ground level. *Water Resources Research*, **11**, 543–550.

— (1975b) The roughness length for water vapor sensible heat, and other scalars. *Journal of Atmospheric Sciences*, **32**, 2028–2031.

— (1982) *Evaporation into the atmosphere: theory, history and applications*, vol. 1. Springer Science & Business Media.

Cai, X.-M. (2012) Effects of wall heating on flow characteristics in a street canyon. *Boundary-Layer Meteorology*, **142**, 443–467.

Castellví, F. (2018) An advanced method based on surface renewal theory to estimate the friction velocity and the surface heat flux. *Water Resources Research*, **54**, 10–134.

Castellvi, F., Snyder, R. and Baldocchi, D. (2008) Surface energy-balance closure over rangeland grass using the eddy covariance method and surface renewal analysis. *Agricultural and Forest Meteorology*, **148**, 1147–1160.

Chen, F. and Zhang, Y. (2009) On the coupling strength between the land surface and the atmosphere: From viewpoint of surface exchange coefficients. *Geophysical Research Letters*, **36**.

Chen, Y., Yang, K., Zhou, D., Qin, J. and Guo, X. (2010) Improving the noah land surface model in arid regions with an appropriate parameterization of the thermal roughness length. *Journal of Hydrometeorology*, **11**, 995–1006.

Chester, S., Meneveau, C. and Parlange, M. B. (2007) Modeling turbulent flow over fractal trees with renormalized numerical simulation. *Journal of Computational Physics*, **225**, 427–448.

Chung, J., Hagishima, A., Ikegaya, N. and Tanimoto, J. (2015) Wind-Tunnel Study of Scalar Transfer Phenomena for Surfaces of Block Arrays and Smooth Walls with Dry Patches. *Boundary-Layer Meteorology*, **157**, 219–236.

Clayson, C. A., Fairall, C. W. and Curry, J. A. (1996) Evaluation of turbulent fluxes at the ocean surface using surface renewal theory. *Journal of Geophysical Research: Oceans*, **101**, 28503.

Crawford, B., Grimmond, S. B., Gabey, A., Marconcini, M., Ward, H. C. and Kent, C. W. (2018) Variability of urban surface temperatures and implications for aerodynamic energy exchange in unstable conditions. *Quarterly Journal of the Royal Meteorological Society*, **144**, 1719–1741.

Danckwerts, P. V. (1951) Significance of liquid-film coefficients in gas absorption. *Industrial & Engineering Chemistry*, **43**, 1460–1467.

De Ridder, K. (2006) Testing brutsaert's temperature roughness parameterization for representing urban surfaces in atmospheric models. *Geophysical Research Letters*, **33**.

564 Demuzere, M., De Ridder, K. and Van Lipzig, N. (2008) Modeling the energy balance in marseille: Sensitivity to roughness
565 length parameterizations and thermal admittance. *Journal of Geophysical Research: Atmospheres*, **113**.

566 Denby, B. and Snellen, H. (2002) A comparison of surface renewal theory with the observed roughness length for temperature
567 on a melting glacier surface. *Boundary-Layer Meteorology*, **103**, 459–468.

568 Flack, K. A. and Schultz, M. P. (2014) Roughness effects on wall-bounded turbulent flows. *Physics of Fluids*, **26**.

569 Fowler, A. J. and Bejan, A. (1995) Forced convection from a surface covered with flexible fibers. *International journal of heat
570 and mass transfer*, **38**, 767–777.

571 Garratt, J. (1980) Surface influence upon vertical profiles in the atmospheric near-surface layer. *Quarterly Journal of the Royal
572 Meteorological Society*, **106**, 803–819.

573 Garratt, J. R. (1992) The atmospheric boundary layer, cambridge atmos. *Space Sci. Ser., Cambridge Univ. Press, Cambridge, UK*.

574 Ghisalberti, M. (2009) Obstructed shear flows: similarities across systems and scales. *Journal of Fluid Mechanics*, **641**, 51–61.

575 Gioia, G., Guttenberg, N., Goldenfeld, N. and Chakraborty, P. (2010) Spectral theory of the turbulent mean-velocity profile.
576 *Physical review letters*, **105**, 184501.

577 Giometto, M. G., Christen, A., Meneveau, C., Fang, J., Krafczyk, M. and Parlange, M. B. (2016) Spatial Characteristics of
578 Roughness Sublayer Mean Flow and Turbulence Over a Realistic Urban Surface. *Boundary-Layer Meteorology*, 1–28.

579 Grimmond, C. and Oke, T. R. (1999) Aerodynamic properties of urban areas derived from analysis of surface form. *Journal of
580 Applied Meteorology*.

581 — (2002) Turbulent heat fluxes in urban areas: Observations and a local-scale urban meteorological parameterization scheme
582 (lumps). *Journal of Applied Meteorology*, **41**, 792–810.

583 Hagishima, A., Tanimoto, J., Nagayama, K. and Meno, S. (2009) Aerodynamic parameters of regular arrays of rectangular blocks
584 with various geometries. *Boundary-Layer Meteorology*, **132**, 315–337.

585 Harman, I. N. and Finnigan, J. J. (2007) A simple unified theory for flow in the canopy and roughness sublayer. *Boundary-Layer
586 Meteorology*, **123**, 339–363.

587 — (2008) Scalar concentration profiles in the canopy and roughness sublayer. *Boundary-Layer Meteorology*, **129**, 323–351.

588 Ikegaya, N., Hagishima, A., Tanimoto, J., Tanaka, Y., Narita, K. and Zaki, S. A. (2012) Geometric Dependence of the Scalar
589 Transfer Efficiency over Rough Surfaces. *Boundary-Layer Meteorology*, **143**, 357–377.

590 Jackson, P. S. (1981) On the displacement height in the logarithmic velocity profile. *Journal of Fluid Mechanics*, **111**, 15.

591 Kader, B. and Yaglom, A. (1972) Heat and mass transfer laws for fully turbulent wall flows. *International Journal of Heat and
592 Mass Transfer*, **15**, 2329–2351.

593 Kanda, M., Inagaki, A., Miyamoto, T., Gryschka, M. and Raasch, S. (2013) A new aerodynamic parametrization for real urban
594 surfaces. *Boundary-Layer Meteorology*, **148**, 357–377.

595 Kanda, M., Kanega, M., Kawai, T., Moriwaki, R. and Sugawara, H. (2007) Roughness lengths for momentum and heat derived
596 from outdoor urban scale models. *Journal of Applied Meteorology and Climatology*, **46**, 1067–1079.

597 Kanda, M., Moriwaki, R. and Kasamatsu, F. (2004) Large-eddy simulation of turbulent organized structures within and above
598 explicitly resolved cube arrays. *Boundary-Layer Meteorology*, **112**, 343–368.

599 Kastner-Klein, P. and Rotach, M. W. (2004) Mean Flow and Turbulence Characteristics in an Urban Roughness Sublayer.
600 *Boundary-Layer Meteorology*, **111**, 55.

Katul, G., Geron, C., Hsieh, C., Vidakovic, B. and Guenther, A. (1998) Active turbulence and scalar transport near the forest–atmosphere interface. *Journal of Applied Meteorology*, **37**, 1533–1546.

Katul, G., Hsieh, C.-I., Oren, R., Ellsworth, D. and Phillips, N. (1996) Latent and sensible heat flux predictions from a uniform pine forest using surface renewal and flux variance methods. *Boundary-Layer Meteorology*, **80**, 249–282.

Katul, G. and Liu, H. (2017) A kolmogorov-brutsaert structure function model for evaporation into a turbulent atmosphere. *Water Resources Research*, **53**, 3635–3644.

Katul, G., Porporato, A., Cava, D. and Siqueira, M. (2006) An analysis of intermittency, scaling, and surface renewal in atmospheric surface layer turbulence. *Physica D: Nonlinear Phenomena*, **215**, 117–126.

Kent, C. W., Grimmond, C., Barlow, J., Gatey, D., Kotthaus, S., Lindberg, F. and Halios, C. H. (2017) Evaluation of Urban Local-Scale Aerodynamic Parameters: Implications for the Vertical Profile of Wind Speed and for Source Areas. *Boundary-Layer Meteorology*, **164**, 1–31.

Leonardi, S. and Castro, I. P. (2010) Channel flow over large cube roughness: a direct numerical simulation study. *Journal of Fluid Mechanics*, **651**, 519.

Leonardi, S., Orlandi, P., Djenidi, L. and Antonia, R. A. (2015) Heat transfer in a turbulent channel flow with square bars or circular rods on one wall. *Journal of Fluid Mechanics*, **776**, 512–530.

Lhomme, J.-P. (1991) The concept of canopy resistance: historical survey and comparison of different approaches. *Agricultural and forest Meteorology*, **54**, 227–240.

Li, D. and Bou-Zeid, E. (2014) Quality and sensitivity of high-resolution numerical simulation of urban heat islands. *Environmental Research Letters*, **9**, 055001.

Li, D., Rigden, A., Salvucci, G. and Liu, H. (2017) Reconciling the Reynolds number dependence of scalar roughness length and laminar resistance. *Geophysical Research Letters*, **44**, 3193–3200.

Li, Q. and Bou-Zeid, E. (2019) Contrasts between momentum and scalar transport over very rough surfaces. *Journal of Fluid Mechanics*, **880**, 32–58.

Li, Q., Bou-Zeid, E. and Anderson, W. (2016a) The impact and treatment of the Gibbs phenomenon in immersed boundary method simulations of momentum and scalar transport. *Journal of Computational Physics*, **310**, 237–251.

Li, Q., Bou-Zeid, E., Anderson, W., Grimmond, C. and Hultmark, M. (2016b) Quality and reliability of les of convective scalar transfer at high reynolds numbers. *International Journal of Heat and Mass Transfer*, **102**, 959–970.

Li, Q., Bou-Zeid, E., Vercauteren, N. and Parlange, M. B. (2018) Signatures of air–wave interactions over a large lake. *Boundary-Layer Meteorology*, **167**, 445–468.

Llaguno-Munitxa, M. and Bou-Zeid, E. (2018) Shaping buildings to promote street ventilation: A large-eddy simulation study. *Urban climate*, **26**, 76–94.

Macdonald, R. W., Griffiths, R. F. and Hall, D. J. (1998) An improved method for the estimation of surface roughness of obstacle arrays. *Atmospheric Environment*, **32**, 1857–1864.

Masson, V. (2000) A physically-based scheme for the urban energy budget in atmospheric models. *Boundary-Layer Meteorology*, **94**, 357–397.

Monin, A. S. and Obukhov, A. M. (1954) Osnovnye zakonomernosti turbulentnogo peremesivanija v prizemnom sloe atmosfery. *Trudy Geofiz. Inst. AN SSSR*, **24**, 163–187.

Moog, D. and Jirka, G. (1999) Air-water gas transfer in uniform channel flow. *Journal of Hydraulic Engineering*, **125**, 3–10.

Moriwaki, R. and Kanda, M. (2006a) Scalar Roughness Parameters for a Suburban Area. *Journal of the Meteorological Society of Japan*, **84**, 1063.

— (2006b) Scalar roughness parameters for a suburban area. *Journal of the Meteorological Society of Japan. Ser. II*, **84**, 1063–1071.

Morrison, W., Yin, T., Lauret, N., Guilleux, J., Kotthaus, S., Gastellu-Etchegorry, J.-P., Norford, L. and Grimmond, S. (2020) Atmospheric and emissivity corrections for ground-based thermography using 3d radiative transfer modelling. *Remote Sensing of Environment*, **237**, 111524.

Nikuradse, J. (1933) Laws of Flow in Rough Pipes - Translation of "Stromungsgesetze in rauhen Rohren". *Tech. rep.*

Owen, P. R. and Thomson, W. (1963) Heat transfer across rough surfaces. *Journal of Fluid Mechanics*, **15**, 321–334.

Perry, A. E., Schofield, W. H. and Joubert, P. N. (1969) Rough wall turbulent boundary layers. *Journal of Fluid Mechanics*, **37**, 383–413.

Placidi, M. and Ganapathisubramani, B. (2015) Effects of frontal and plan solidities on aerodynamic parameters and the roughness sublayer in turbulent boundary layers. *Journal of Fluid Mechanics*, **782**, 541–566.

Poggi, D., Porporato, A., Ridolfi, L., Albertson, J. and Katul, G. (2004) The effect of vegetation density on canopy sub-layer turbulence. *Boundary-Layer Meteorology*, **111**, 565–587.

Pope, S. B. (2000) *Turbulent flows*. Cambridge: Cambridge University Press.

Raupach, M. R., Finnigan, J. J. and Brunei, Y. (1996) Coherent eddies and turbulence in vegetation canopies: The mixing-layer analogy. *Boundary-Layer Meteorology*, **78**, 351–382.

Ryu, Y. H., Baik, J. J. and Lee, S. H. (2011) A new single-layer urban canopy model for use in mesoscale atmospheric models. *Journal of Applied Meteorology and Climatology*, **46**, 1067–1079.

Schmugge, T., Kustas, W., Ritchie, J., Jackson, T. and Rango, A. (2002) Remote sensing in hydrology. *Advances in Water Resources*, **25**, 1367–1385.

Siqueira, M. B. and Katul, G. G. (2010) An analytical model for the distribution of co 2 sources and sinks, fluxes, and mean concentration within the roughness sub-layer. *Boundary-Layer Meteorology*, **135**, 31–50.

Slotnick, J., Khodadoust, A., Alonso, J., Darmofal, D., Gropp, W., Lurie, E. and Mavriplis, D. (2014) Cfd vision 2030 study: a path to revolutionary computational aerosciences. *NASA Tech. Rep. CR-2014-218178, Langley Res. Cent., Hampton, VA*.

Snyder, R., Spano, D. and Pawu, K. (1996) Surface renewal analysis for sensible and latent heat flux density. *Boundary-Layer Meteorology*, **77**, 249–266.

Sullivan, P. P., Banner, M. L., Morison, R. P. and Peirson, W. L. (2017) Turbulent Flow over Steep Steady and Unsteady Waves under Strong Wind Forcing. *Journal of Physical Oceanography*, **48**, 3–27.

Theeuwes, N. E., Ronda, R. J., Harman, I. N., Christen, A. and Grimmond, C. S. B. (2019) Parametrizing horizontally-averaged wind and temperature profiles in the urban roughness sublayer. *Boundary-Layer Meteorology*, **173**, 321–348.

Tseng, Y. H., Meneveau, C. and Parlange, M. B. (2006) Modeling flow around bluff bodies and predicting urban dispersion using large eddy simulation. *Environmental Science & Technology*, **40**, 2653–2662.

Voogt, J. A. and Grimmond, C. S. B. (2000) Modeling Surface Sensible Heat Flux Using Surface Radiative Temperatures in a Simple Urban Area. *Journal of Applied Meteorology*, **39**, 1679.

Wang, Z.-H., Bou-Zeid, E. and Smith, J. A. (2013) A coupled energy transport and hydrological model for urban canopies evaluated using a wireless sensor network. *Quarterly Journal of the Royal Meteorological Society*, **139**, 1643–1657.

677 Yang, X., Hu, H., Huang, X. and Ge, M. (2019) Drag forces on sparsely packed cube arrays. *Journal of Fluid Mechanics*.

678 Yang, X. I. and Abkar, M. (2018) A hierarchical random additive model for passive scalars in wall-bounded flows at high
679 Reynolds numbers. *Journal of Fluid Mechanics*.

680 Yang, X. I. A., Sadique, J., Mittal, R. and Meneveau, C. (2016) Exponential roughness layer and analytical model for turbulent
681 boundary layer flow over rectangular-prism roughness elements. *Journal of Fluid Mechanics*, **789**, 127.

682 Zhu, X. and Anderson, W. (2018) Turbulent flow over urban-like fractals: prognostic roughness model for unresolved genera-
683 tions. *Journal of Turbulence*, **19**, 995–1016.

684 Zhu, X., Iungo, G. V., Leonardi, S. and Anderson, W. (2017) Parametric study of urban-like topographic statistical moments
685 relevant to a priori modelling of bulk aerodynamic parameters. *Boundary-Layer Meteorology*, **162**, 231–253.

686 Zilitinkevich, S. S., Grachev, A. A. and Fairall, C. W. (2001) Notes and correspondece: Scaling reasoning and field data on the
687 sea surface roughness lengths for scalars. *Journal of the Atmospheric Sciences*, **58**, 320–325.